CHALMERS
UNIVERSITY OF TECHNOLOGY

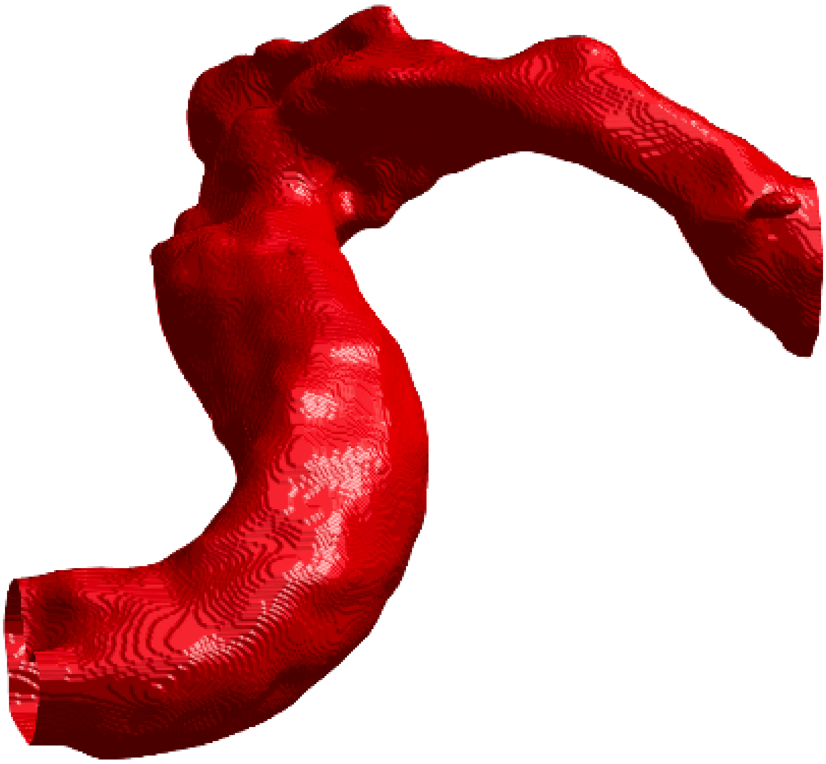

Computational Fluid Dynamics of Human Cerebral Circulation

A Study of Shear Stress in the Circle of Willis with and without Constructed Aneurysms

Bachelor's thesis in Mechanical Engineering

AMIR ABASS
KAJSA AHLGREN
CARL ANDERSSON
HENRIK BERGGREN
VICTORIA IGNELL
VILMA KOIVISTOINEN

Department of Mechanics and Maritime Sciences
CHALMERS UNIVERSITY OF TECHNOLOGY
Gothenburg, Sweden 2019

Bachelor's thesis 2019:07

Computational Fluid Dynamics of Human Cerebral Circulation

A Study of Shear Stress in the Circle of Willis with and without Constructed Aneurysms

Amir Abass | Kajsa Ahlgren | Carl Andersson | Henrik Berggren
Victoria Ignell | Vilma Koivistoinen

Department of Mechanics and Maritime Sciences
Division of Fluid Dynamics
Chalmers University of Technology
Gothenburg, Sweden 2019

Computational Fluid Dynamics of Human Cerebral Circulation
A Study of Shear Stress in the Circle of Willis with and without Constructed Aneurysms
Amir Abass, Kajsa Ahlgren, Carl Andersson, Henrik Berggren, Victoria Ignell, Vilma Koivistoinen

Supervisor: Dario Maggiolo, Department of Mechanics and Maritime Sciences
Examiner: Srdjan Sasic, Department of Mechanics and Maritime Sciences

Bachelor's Thesis 2019:07
Department of Mechanics and Maritime Sciences
Division of Fluid Dynamics
Chalmers University of Technology
SE-412 96 Gothenburg
Telephone +46 31-772 10 00

Cover: Reconstructed artery near Rt ICA in the Circle of Willis, used for simulations.

Abstract

A cerebral aneurysm is a local enlargement of a weakened blood vessel wall in the brain. It is a critical condition that causes several deaths yearly due to the fatal intracranial bleeding that a rupture of an aneurysm can cause. This report investigates aneurysms with focus on their impact on shear stress in blood vessels where aneurysms are often found. This is done with the aim to gain further knowledge about the correlation between mechanical factors and aneurysm progression.

Throughout the report images of brains from two healthy patients, taken with magnetic resonance imaging, serve as a fundamental basis of real-world representation of blood vessels in the human brain. The scanned images were reconstructed into three-dimensional volumetric data to use for simulations. A total of seven specific vascular geometries were chosen from the two brains. All were selected in the Circle of Willis, a specific section in the lower central part of the brain. The Circle of Willis is a domain particularly prone to the development of aneurysms. Since the images originated from healthy patients the chosen geometries did not contain any aneurysms. Therefore a modified copy of each selected geometry was created as well, with the difference being that they contained a virtually inserted aneurysm.

The blood flow of the reconstructed vascular geometries was computed and simulated using the Lattice Boltzmann method. It is a numerical method that recovers the Navier-Stokes continuity and generates the velocity field within the chosen blood vessel geometries. The blood flow was simulated in all seven pairs of blood vessels. With the acquisition of the velocity distribution within the vessel, the corresponding distribution of shear stress was calculated. Results from the simulations were compared between the cases with and without aneurysm with respect to shear stress. The concluding result was that a global increase in shear stress was found for the geometries with an aneurysm. This result suggests that the progression of one aneurysm could lead to a weakened blood vessel that is likely to develop an increased number of aneurysms.

Keywords: Lattice Boltzmann, Cerebral aneurysm, Cerebral circulation, CFD, Vascular system

Sammanfattning

Artärbråck, även kallat aneurysm, är en lokal utvidgning av en försvagad blodkärlsvägg i hjärnan. Det är ett allvarligt tillstånd som orsakar många dödsfall varje år på grund av den livshotande hjärnblödning som sprickning av aneurysmer kan orsaka. Denna rapport undersöker aneurysmer med fokus på dess inverkan på skjuvspänningen i blodkärl där aneurysmer ofta bildas. Detta görs med målet att få ökad kunskap i korrelationen mellan mekaniska faktorer och aneurysmbildning.

Genom rapporten används magnetröntgenbilder av hjärnor från två friska patienter som underlag till verklighetsbaserade representationer av blodkärl i den mänskliga hjärnan. Magnetröntgenbilderna rekonstruerades till tredimensionell volymetrisk data för att användas i simuleringar. Totalt valdes sju specifika blodkärlsgeometrier från de två hjärnorna. Alla valdes i Willis ring, ett specifikt område i den nedre, centrala delen av hjärnan. Willis ring är ett område där aneurysmer ofta utvecklas. Eftersom magnetröntgenbilderna härrörde från friska människor innehöll ingen av de valda rekonstruerade geometrierna någon aneurysm. Utöver detta framställdes ytterligare en uppsättning av samma geometrier, med skillnaden att en virtuellt konstruerad aneurysm placerades in i varje blodkärl.

Blodflödet i rekonstruerade utvalda delar av hjärnan beräknades och simulerades med Lattice Boltzmann-metoden. Det är en numerisk metod som återger lösningarna till Navier-Stokes kontinuiteten och genererar hastighetsfältet i de utvalda blodkärlen. Blodflödet simulerades i alla sju par av blodkärl. Utifrån den resulterande hastighetsfördelningen i blodkärlet kunde den motsvarande fördelningen av skjuvspänningen räknas ut. Resultaten från simuleringarna jämfördes med avseende på skjuvspänning i fallen med och utan aneurysm. Det slutliga resultatet av detta var att en global ökning av skjuvspänning tillkom i blodkärl med aneurysm. Detta tyder på att uppkomsten av en aneurysm kan bidra till en ökad försvagning av blodkärl med förhöjd risk för utveckling av ytterligare aneurysmer.

Acknowledgements

First and foremost we would like to thank our supervisor Dario Maggiolo for the unselfish way he has shared his knowledge of both advanced and not so advanced subjects in writing this report. His commitment and support has been key for the project.

Furthermore we would also like to acknowledge Chalmers Centre for Computational Science and Engineering (C3SE) for their guidance in the use of the cluster at Chalmers University of Technology.

A special thanks goes to the staff at the Chalmers main library for their help with the reference system.

Lastly we would like to thank whoever invented the Swedish tradition of *fika*, keeping our spirits high during the long days.

Amir Abass, Kajsa Ahlgren, Carl Andersson, Henrik Berggren, Victoria Ignell, Vilma Koivistoinen, Gothenburg, May 2019

Contents

1 Introduction

The study of the correlation between flow characteristics and diseases in the human vascular system has increased in the last years [1, 2, 3, 4]. This is mostly due to the advancement of Computational Fluid Dynamics (CFD) and the development of numerical tools, allowing for complex reconstructions of the vascular systems to be created virtually. These improvements enable the examination of the impact of hemodynamics, the dynamics of the blood flow, on the progression of diseases in the vascular system.

The general technique of modeling, simulating and visualizing biological processes computationally in a virtual environment is called *in silico*, where use of the Lattice Boltzmann method (LBM) to generate velocity field solutions is one example of this technique. The Lattice Boltzmann method is one class of CFD methods. It solves fluid flow problems numerically with a mesoscopic approach by considering the behavior of particles as a distribution instead of modelling every single particle [5]. *In silico* techniques make use of mathematical models and biological data available from past studies and experiments. It is an alternative method of investigating pathology on the human body and differs from *in vivo* which involves direct testing of living organisms. *In vivo* studies are most often performed on animals whose physiological differences from humans could lead to inaccuracies in results. The use of animals in medical and biological research is still a topic of debate. See section 6.3 for a longer ethical discussion on how the use of *in silico* techniques, such as in this project, can impact the future of biological research.

Current computational hemodynamic studies have shown that certain flow patterns have a strong link to specific diseases and physical disorders. Two examples are cancer and cerebral aneurysms where the former focuses on distribution and progression of cancer cells [1], and the latter on the initiation and rupture of cerebral aneurysms [6, 7]. More severe and common diseases such as stroke, the second cause of death globally [8], can also be linked to hemodynamics [2].

Cerebral or intracranial aneurysms can be divided into four subgroups: saccular, fusiform, dissecting and mycotic. Saccular aneurysms, characterized by round bulges that protrude from only one side of the blood vessel wall, are the most common of these four [9].

The aneurysm progression is a noticeably active area of research because of its mechanical and biological complexity. Intracranial aneurysms are most common in the Circle of Willis (CoW) which is a circle of communicating arteries at the base of the brain [2]. Subarachnoid hemorrhage (SAH), one of the most severe types of stroke, occurs when an intracranial aneurysm ruptures [10]. Therefore research about aneurysms and associated hemodynamic mechanical factors such as wall shear stress (WSS) in the CoW is of high interest and could pave way to improved methods of preventing and treating aneurysms that pose a risk to the bearer.

1.1 Objective of Study

The overall aim of this work is to explore the correlation between flow characteristics and diseases found in the vascular system of humans. The study will focus on investigating how aneurysms affect shear stress in the CoW with the use of the Lattice Boltzmann methodology.

1.2 Purpose and Scope

As stated in the introduction, SAH is one of the most severe types of strokes and is often fatal. Therefore there exist strong incentives to investigate the cause and development of aneurysms. The methods used in this project, namely the use of *in silico* techniques, is also of interest from the perspective of utilizing alternative methods in medical and biological research. This project could contribute to the building of further trust in *in silico* techniques and the eventual reduction of animal testing.

In order to investigate the effects from a constructed aneurysm, geometries from two human brains of healthy patients are reconstructed. An open-source magnetic resonance imaging (MRI) data base [11] is used to acquire images of the two brains. The reconstruction of volumetric data from each of the image sets is done in MATLAB, this is described in depth in section 4.1. The geometries are also modified by the insertion of a constructed aneurysm, to draw comparisons of the shear stress between geometries with and without an inserted aneurysm.

This report focuses on the vascular system of the human brain. The Circle of Willis is selected as the area of interest in the brain, seeing as it is the location for 85% of all saccular aneurysms [9]. Within the CoW, seven independent arteries are selected from the available brains, these are presented in section 4.2. Here the targeted condition is the progression of aneurysms. Due to how common they are, saccular aneurysms are chosen when virtually inserting aneurysms in the selected geometries. Furthermore, this report exclusively focuses on the impact of shear stress in the connection between flow characteristics and aneurysm progression.

2 Theory of Fluid Dynamics and the Lattice Boltzmann Method

Herein are described concepts and theories that form the basis for the simulations. This includes a description of the Lattice Boltzmann method that is used for the simulations and Hagen-Poiseuille flow that is used for subsequent validation of the MATLAB code.

2.1 Reynolds Number

The Reynolds number (Re) is a dimensionless quantity in fluid mechanics which is used to characterize various cases of flow. The physical meaning of Re may be described as a relation between the interstitial force and the viscous force. Equation (1) describes the Reynolds number [12].

$$\mathrm{Re} = \frac{L\rho u}{\mu} = \frac{Lu}{\nu} \tag{1}$$

Here ρ is the fluid density, u is the velocity of the fluid, L is the characteristic length, μ and ν is the dynamic and kinematic viscosity of the fluid. The critical point in pipe flow occurs when Re approaches 2100. Thus, the flow is laminar when $\mathrm{Re} < 2100$ and turbulent when $\mathrm{Re} > 4000$.

2.2 Law of Hagen-Poiseuille

The law of Hagen-Poiseuille describes the incompressible laminar fluid flow in a pipe with a constant cross section area and is given by

$$-\frac{dP}{dx} = \frac{8\mu u_{avg}}{R^2} = \frac{32\mu u_{avg}}{D^2} \tag{2}$$

where R is the pipe radius and D is the pipe diameter. Equation (2) is known as the Hagen-Poiseuille equation [12]. The expression correlates the pressure drop over a given length to the drag force on the pipe resulting from the flow of a fluid.

Whilst using the Hagen-Poiseuille equation it is essential to know that there are conditions on both the fluid and the flow that should be met. For instance the fluid is to be Newtonian and behave as a continuum. Furthermore, the flow should be laminar, steady, fully developed and incompressible.

Equation (3) describes the velocity profile for fully developed flow in a pipe in three dimensions [12], with the same notations as for equation (2).

$$u_x = -\frac{dP}{dx}\frac{R^2}{4\mu}\left(1 - \left(\frac{r}{R}\right)^2\right) \tag{3}$$

Here the parameter r is the distance from the midpoint of the pipe. For equation (3) the flow is assumed to be laminar and the fluid is assumed to be Newtonian. A no-slip condition is applied, therefore the velocity at the walls is zero. Moreover, the profile of the shear stress, τ, in a pipe can be obtained with equation (4) [12].

$$\tau_{rx} = \left(\frac{dP}{dx}\right)\frac{r}{2} \tag{4}$$

The velocity profile for flow between two parallel plates is described by equation (5) [13].

$$u = -\frac{dP}{dx}\frac{H^2}{2\mu}\left(1 - \frac{y^2}{H^2}\right) \tag{5}$$

In equation (5) the origin is defined in the middle of the two plates. The parameter y is the distance from the origin and H is the total distance from the origin to the plate.

If the fluid is Newtonian equation (6) [12] can be used to calculate the shear stress.

$$\tau_{yx} = \mu\frac{du_x}{dy} \tag{6}$$

The profile for shear stress regarding flow between two parallel plates is obtained by deriving equation (5) with respect to y and using equation (6) which gives equation (7).

$$\tau_{yx} = y\frac{dP}{dx} \tag{7}$$

2.3 Stokes Flow

Stokes flow, also known as creeping flow, is a phenomenon that occurs in a fluid flow when advective inertial forces are small relative to viscous forces [14]. Moreover, Stokes flow is usually characterized by the Reynolds number being extremely low, Re $\ll 1$ [15]. As may be noted by studying equation (1), a small Reynolds number will be achieved by possessing a small characteristic length, a fluid flowing at a low velocity or by having a very viscous fluid [15]. The equations given in (8) are known as the incompressible Navier-Stokes equations [16].

$$\begin{aligned} \nabla \cdot \vec{V} &= 0 \\ \frac{\partial \vec{V}}{\partial t} + (\vec{V} \cdot \nabla)\vec{V} &= -\frac{1}{\rho}\nabla p + v\nabla^2\vec{V} \end{aligned} \tag{8}$$

In cases when Re $\ll 1$ the term $(\vec{V} \cdot \nabla)\vec{V}$, that describes convective acceleration, may be neglected which results in the Stokes equation, a linearized form of the Navier-Stokes equations specifically describing creeping motion of a fluid [16]. Thus the second equation in (8) becomes equation (9).

$$\frac{\partial \vec{V}}{\partial t} = -\frac{1}{\rho}\nabla p + v\nabla^2\vec{V} \tag{9}$$

This means that all fluid flows that satisfy equation (9) are considered to have creeping motion. Moreover, it is mostly in smaller vessels and capillaries that creeping flow occur whereas in larger arteries the flow is generally laminar with the possibility of minor secondary flows, especially in regions of branching and curvature [17].

Stokes flow contributes to a time reversal symmetry [15] which makes it easier to numerically compute the equation of the flow. The majority of all physical processes behave with asymmetry of time, meaning that the process acts different if the direction of time is positive or negative. A positive direction of time implies going forward in time and the reverse applies for the negative direction. However, symmetry of time on a microscopic level affect a physical process to behave in the same way regardless of the direction of time [18].

2.4 Lattice Boltzmann Method

As stated in the problem description the main aim of the project is to investigate how aneurysms affect shear stress in blood vessels. The absolute data that quantifies the flow characteristics is the velocity distribution within the chosen artery. From this it is possible to visualize the specific movement of the hypothetical blood within the vein, and also to determine the related shear stress. To simulate the velocity distribution in the chosen geometry the Lattice Boltzmann method (LBM) will be used.

2.4.1 Theoretical Idea of the Lattice Boltzmann Method

Usually numerical models have one of the following approaches: the macroscopic approach like Navier-Stokes equations, which takes larger phenomenon into consideration, or the molecular approach which takes the dynamics between molecules into consideration [5]. One property of LBM is that it utilizes both of the above mentioned approaches: a mesoscopic middlepoint. To achieve this, LBM is based on the Boltzmann equation which describes the mechanics of collision and movement of particle probability distributions [19]. The central idea of LBM is the bottom up strategy where equations from the molecular approach are reformulated to the macroscopic approach via local thermodynamic equilibrium [5]. It has been shown that this reformulation recovers the Navier-Stokes continuity [20].

2.4.2 Model Specification

The LBM relies on solving the same equation in numerous amounts of nodes, or cartesian points, in a geometry; which in this case is a reconstructed blood vessel geometry. For a good resolution of the geometry that contains a satisfying amount of nodes compared to the size of the geometry, it is possible to get a good approximation of the flow with discrete velocity values calculated at the nodes. Throughout the report, model MRT-D3Q19 of the Lattice Boltzmann method will be used. This is a special case of LBM where a multiple relaxation time (MRT) factor is used for the collision operator, see equation (14). The lattice of the method is specified as D3Q19, three dimensions and 19 lattice directions, or speeds, that are considered. These 19 lattice directions form a distribution of particle velocities in a node where direction n holds a value that indicates the number of particles currently moving in direction $\mathbf{e}_n$. in the current node, with $\mathbf{e}$ being a combinatorial matrix of the 19 direction combinations, as seen here:

$$\mathbf{e} = \begin{bmatrix} 0 & 1 & -1 & 0 & 0 & 0 & 0 & 1 & -1 & 1 & -1 & 1 & -1 & 1 & -1 & 0 & 0 & 0 & 0 \\ 0 & 0 & 0 & 1 & -1 & 0 & 0 & 1 & 1 & -1 & -1 & 0 & 0 & 0 & 0 & 1 & -1 & 1 & -1 \\ 0 & 0 & 0 & 0 & 0 & 1 & -1 & 0 & 0 & 0 & 0 & 1 & 1 & -1 & -1 & 1 & 1 & -1 & -1 \end{bmatrix}^{\mathrm{T}}$$

Here the columns specify the three dimensions and the different lattice directions are found in each row of $\mathbf{e}$. All vector directions are visualized in figure 1 in section 2.5.

LBM is an iterative method with time relaxation, the time required for a system to reach equilibrium, in every step for every iteration. Here the velocity is the sum over all lattice directions i, as shown in the following equation

$$\mathbf{u}_j = \frac{1}{\rho} \sum_i \mathbf{e}_{i,j} f_i(\mathbf{x}, t) \tag{10}$$

where ρ is defined as

$$\rho = \sum_i f_i(\mathbf{x}, t). \tag{11}$$

In the equations above f is a probability density function, the probable number of particles in a given thermodynamic volume [5]. With this first calculation of velocities it is possible to calculate f^{eq}, the probability density function at local thermodynamical equilibrium, as

$$f^{eq} = \mathbf{EQ} \cdot \mathbf{V}. \tag{12}$$

Here the matrices EQ and V are defined as following:

$$\mathbf{EQ} = \begin{bmatrix}
1 & 0 & 0 & 0 & 0 & 0 & 0 & 0 & 0 & 0 \\
-11 & 0 & 0 & 0 & \frac{19}{\rho_g} & \frac{19}{\rho_g} & \frac{19}{\rho_g} & 0 & 0 & 0 \\
3 & 0 & 0 & 0 & -\frac{11}{2\rho_g} & -\frac{11}{2\rho_g} & -\frac{11}{2\rho_g} & 0 & 0 & 0 \\
0 & 1 & 0 & 0 & 0 & 0 & 0 & 0 & 0 & 0 \\
0 & -\frac{2}{3} & 0 & 0 & 0 & 0 & 0 & 0 & 0 & 0 \\
0 & 0 & 1 & 0 & 0 & 0 & 0 & 0 & 0 & 0 \\
0 & 0 & -\frac{2}{3} & 0 & 0 & 0 & 0 & 0 & 0 & 0 \\
0 & 0 & 0 & 1 & 0 & 0 & 0 & 0 & 0 & 0 \\
0 & 0 & 0 & -\frac{2}{3} & 0 & 0 & 0 & 0 & 0 & 0 \\
0 & 0 & 0 & 0 & \frac{2}{\rho_g} & -\frac{1}{\rho_g} & -\frac{1}{\rho_g} & 0 & 0 & 0 \\
0 & 0 & 0 & 0 & -\frac{1}{\rho_g} & -\frac{1}{2\rho_g} & \frac{1}{2\rho_g} & 0 & 0 & 0 \\
0 & 0 & 0 & 0 & 0 & \frac{1}{\rho_g} & -\frac{1}{\rho_g} & 0 & 0 & 0 \\
0 & 0 & 0 & 0 & 0 & -\frac{1}{2\rho_g} & \frac{1}{2\rho_g} & 0 & 0 & 0 \\
0 & 0 & 0 & 0 & 0 & 0 & 0 & \frac{1}{\rho_g} & 0 & 0 \\
0 & 0 & 0 & 0 & 0 & 0 & 0 & 0 & \frac{1}{\rho_g} & 0 \\
0 & 0 & 0 & 0 & 0 & 0 & 0 & 0 & 0 & \frac{1}{\rho_g} \\
0 & 0 & 0 & 0 & 0 & 0 & 0 & 0 & 0 & 0 \\
0 & 0 & 0 & 0 & 0 & 0 & 0 & 0 & 0 & 0 \\
0 & 0 & 0 & 0 & 0 & 0 & 0 & 0 & 0 & 0
\end{bmatrix}, \quad \mathbf{V} = \begin{bmatrix}
\rho \\ u_x \\ u_y \\ u_z \\ u_x^2 \\ u_y^2 \\ u_z^2 \\ u_x u_y \\ u_x u_z \\ u_y u_z
\end{bmatrix}. \tag{13}$$

Using f^{eq} the effects of collision within the probability density function can be modelled. In MRT-D3Q19, this is done according to the collision operator equation (14) where the resulting probability density function after collision is denoted f^+ [21].

$$f^+ = f - M^{-1} S \left(Mf - f^{eq} \right) \tag{14}$$

The M-matrix above is a transformation matrix that projects f, $f^{eq} \in \mathbb{V}$, where $\mathbb{V}$ is the vector space of discrete velocities, to the space of $\mathbb{R}^b$ [22]. The explicit version of M is given below:

$$M = \begin{bmatrix} 1 & 1 & 1 & 1 & 1 & 1 & 1 & 1 & 1 & 1 & 1 & 1 & 1 & 1 & 1 & 1 & 1 & 1 & 1 \\ -30 & -11 & -11 & -11 & -11 & -11 & -11 & 8 & 8 & 8 & 8 & 8 & 8 & 8 & 8 & 8 & 8 & 8 & 8 \\ 12 & -4 & -4 & -4 & -4 & -4 & -4 & 1 & 1 & 1 & 1 & 1 & 1 & 1 & 1 & 1 & 1 & 1 & 1 \\ 0 & 1 & -1 & 0 & 0 & 0 & 0 & 1 & -1 & 1 & -1 & 1 & -1 & 1 & -1 & 0 & 0 & 0 & 0 \\ 0 & -4 & 4 & 0 & 0 & 0 & 0 & 1 & -1 & 1 & -1 & 1 & -1 & 1 & -1 & 0 & 0 & 0 & 0 \\ 0 & 0 & 0 & 1 & -1 & 0 & 0 & 1 & 1 & -1 & -1 & 0 & 0 & 0 & 0 & 1 & -1 & 1 & -1 \\ 0 & 0 & 0 & -4 & 4 & 0 & 0 & 1 & 1 & -1 & -1 & 0 & 0 & 0 & 0 & 1 & -1 & 1 & -1 \\ 0 & 0 & 0 & 0 & 0 & 1 & -1 & 0 & 0 & 0 & 0 & 1 & 1 & -1 & -1 & 1 & 1 & -1 & -1 \\ 0 & 0 & 0 & 0 & 0 & -4 & 4 & 0 & 0 & 0 & 0 & 1 & 1 & -1 & -1 & 1 & 1 & -1 & -1 \\ 0 & 2 & 2 & -1 & -1 & -1 & -1 & 1 & 1 & 1 & 1 & 1 & 1 & 1 & 1 & -2 & -2 & -2 & -2 \\ 0 & -4 & -4 & 2 & 2 & 2 & 2 & 1 & 1 & 1 & 1 & 1 & 1 & 1 & 1 & -2 & -2 & -2 & -2 \\ 0 & 0 & 0 & 1 & 1 & -1 & -1 & 1 & 1 & 1 & 1 & -1 & -1 & -1 & -1 & 0 & 0 & 0 & 0 \\ 0 & 0 & 0 & -2 & -2 & 2 & 2 & 1 & 1 & 1 & 1 & -1 & -1 & -1 & -1 & 0 & 0 & 0 & 0 \\ 0 & 0 & 0 & 0 & 0 & 0 & 0 & 1 & -1 & -1 & 1 & 0 & 0 & 0 & 0 & 0 & 0 & 0 & 0 \\ 0 & 0 & 0 & 0 & 0 & 0 & 0 & 0 & 0 & 0 & 0 & 0 & 0 & 0 & 0 & 1 & -1 & -1 & 1 \\ 0 & 0 & 0 & 0 & 0 & 0 & 0 & 0 & 0 & 0 & 0 & 1 & -1 & -1 & 1 & 0 & 0 & 0 & 0 \\ 0 & 0 & 0 & 0 & 0 & 0 & 0 & 1 & -1 & 1 & -1 & -1 & 1 & -1 & 1 & 0 & 0 & 0 & 0 \\ 0 & 0 & 0 & 0 & 0 & 0 & 0 & -1 & -1 & 1 & 1 & 0 & 0 & 0 & 0 & 1 & -1 & 1 & -1 \\ 0 & 0 & 0 & 0 & 0 & 0 & 0 & 0 & 0 & 0 & 0 & 1 & 1 & -1 & -1 & -1 & -1 & 1 & 1 \end{bmatrix}$$

2.4.3 Stability of the Lattice Boltzmann Method

The LBM is ensured to be stable with a stated, fixed Reynolds number below one [5]. To model higher Reynolds numbers, the method would need to be stabilized by increasing the resolution of the geometry, as higher resolution decreases the probability for divergent or errant solutions [23]. Other variables that have an impact on the stability is the relaxation time and the magnitude of any driving force used in the simulation. A decreased relaxation time and an increased body force will both affect the stability negatively [5].

2.5 Shear Rate

Shear rate in flows has been found to be derivable from the probability density function [24]. The strain rate tensor is therein defined as the signed sum of relevant density distributions $f^{(1)}$ with the sign depending on the tensor directions $\alpha\beta$, or in other words $\mathbf{e}_{i\alpha}\mathbf{e}_{i\beta}$. Here $\mathbf{e}_{i\alpha}\mathbf{e}_{i\beta}$ takes values of either -1, 0 or 1. For the MRT-D3Q19 model, the variant equation (15) modified from [25] replaces it, implementing the MRT factors.

$$S_{\alpha\beta} = -\frac{1}{2c_s^2\delta t}\sum_i \mathbf{e}_{i\alpha}\mathbf{e}_{i\beta}\sum_j \left(\mathrm{M}^{-1}\mathrm{S}\right)_{i,j}\left(\left(\mathrm{M}f\right)_j - f_{eq,j}\right) \tag{15}$$

Figure 1 demonstrates how this is calculated. For each combination of $\alpha : (x, y, z)$ and $\beta : (x, y, z)$ the contributing versors are colored according to contribution sign: red for positive ($\mathbf{e}_{i\alpha}\mathbf{e}_{i\beta} = 1$), blue for negative ($\mathbf{e}_{i\alpha}\mathbf{e}_{i\beta} = -1$) and black for non-contributing ($\mathbf{e}_{i\alpha}\mathbf{e}_{i\beta} = 0$).

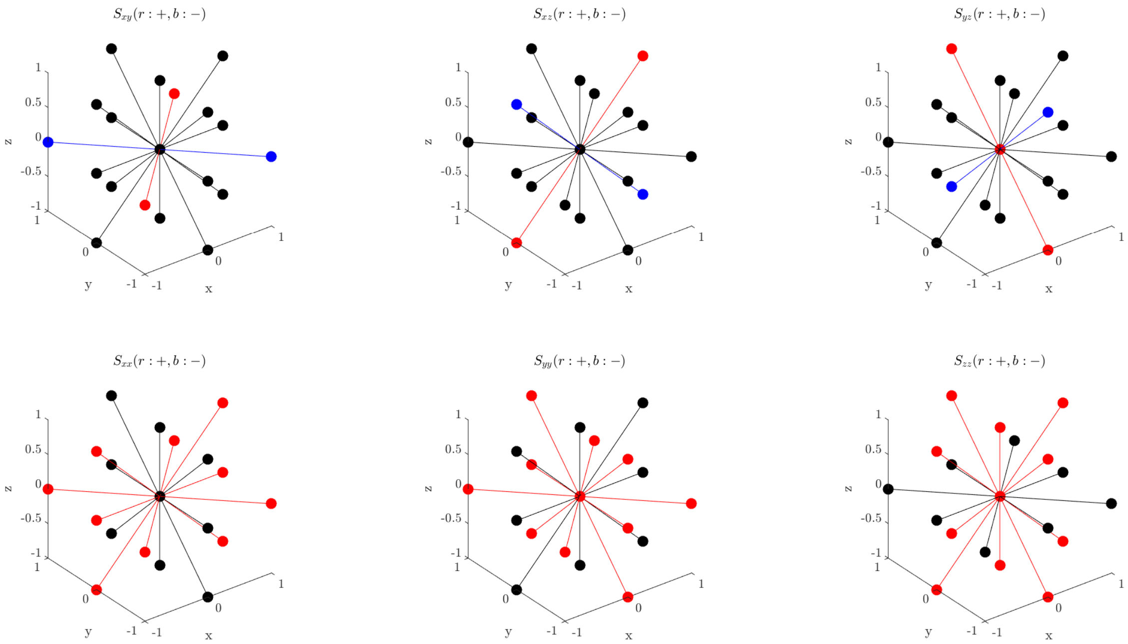

Figure 1: Contributing versors for strain rate tensor calculation (authors' own image)

Given the strain rate tensor, the shear rate $\dot{\gamma}$ is defined according to equation (16) [24].

$$\dot{\gamma} = 2\sqrt{\sum_{\alpha,\beta=1}^{3} S_{\alpha\beta}S_{\alpha\beta}} \tag{16}$$

With the shear rate, the shear stress is defined as $\tau = \dot{\gamma}\mu$ for Newtonian fluids [12].

2.6 Conversion between Lattice Boltzmann-Units and Physical Units

When using the LBM the parameters will be in Lattice Boltzmann-units (LB-units) and it therefore requires a conversion to physical, SI units. Shear stress is one parameter which needs a unit conversion. The ratio between the simulated shear stress in LB-units and SI units should be equal to the ratio between theoretical shear stress for a three-dimensional pipe in LB-units and SI units. This results in equation (17).

$$\frac{\tau_{LB}}{\tau_{ph}} = \frac{\tau_{th,LB}}{\tau_{th,ph}} \tag{17}$$

Here τ is the shear stress, the subscript ph denotes the physical case and LB the Lattice Boltzmann case. The subscript th indicates a theoretical shear stress for a three-dimensional pipe.

The theoretical shear stress in equation (17) can be expressed by equation (4). The shear stress from the simulation, in SI units, can then be written as equation (18).

$$\tau_{ph} = \frac{\tau_{th,ph}}{\tau_{ph}} \cdot \tau_{LB} = \frac{\frac{R_{th,ph}}{2}\left(\frac{dP}{dL}\right)_{th,ph}}{\frac{R_{th,LB}}{2}\left(\frac{dP}{dL}\right)_{th,LB}} \cdot \tau_{LB} \tag{18}$$

Here $\frac{dP}{dL}$ is the pressure gradient. The quotient of the pressure gradients can be expressed with the help of the Reynolds number since it is dimensionless. The Reynolds number will be equal in both form of units and this leads to equation (19).

$$\mathrm{Re}_{th,ph} = \mathrm{Re}_{th,LB} \tag{19}$$

Thereafter the equation for the Reynolds number, see equation (1), can be used. After rewriting, it leads to equation (20).

$$\frac{u_{th,ph}}{u_{th,LB}} = \frac{L_{th,LB} \cdot \rho_{th,LB} \cdot \mu_{th,ph}}{\mu_{th,LB} \cdot \rho_{th,ph} \cdot \mu_{th,LB}} \tag{20}$$

The velocities can be expressed with the help of the Hagen-Poiseuille equation, see equation (2), since it is the theoretical velocities for a three-dimensional pipe in different units. This gives equation (21).

$$\frac{\left(\frac{dP}{dL}\right)_{th,ph}}{\left(\frac{dP}{dL}\right)_{th,LB}} = \frac{R_{th,LB}^2 \cdot L_{th,LB} \cdot \rho_{th,LB} \cdot \mu_{th,ph}^2}{R_{th,ph}^2 \cdot \mu_{th,LB} \cdot \rho_{th,ph} \cdot \mu_{th,LB}^2} \tag{21}$$

Equation (21) can be used in equation (18) which results in equation (22).

$$\tau_{ph} = \frac{R_{th,LB} \cdot L_{th,LB} \cdot \rho_{th,LB} \cdot \mu_{th,ph}^2}{R_{th,ph} \cdot L_{th,ph} \cdot \rho_{th,ph} \cdot \mu_{th,LB}^2} \cdot \tau_{LB} \tag{22}$$

The radius, R, and the characteristic length, L, can be converted between the different units by using the resolution of the geometry, in this case denoted with s. This is shown in equation (23).

$$\begin{aligned} R_{th,ph} &= s \cdot R_{th,LB} \\ L_{th,ph} &= s \cdot L_{th,LB} \end{aligned} \tag{23}$$

When using the relation with the resolution, equation (22) can be written as equation (24).

$$\tau_{ph} = \frac{1}{s^2} \cdot \frac{1}{\rho_{th,ph}} \cdot \frac{\mu_{th,ph}^2}{\mu_{th,LB}^2} \cdot \tau_{LB} \tag{24}$$

The pressure gradient can also be converted between LB-units and SI units by using the Reynolds number and equation (19). The velocity in SI units can be expressed by equation (25).

$$u_{ph} = \frac{u_{LB} \cdot L_{LB} \cdot \rho_{LB} \cdot \mu_{ph}}{L_{ph} \cdot \rho_{ph} \cdot \mu_{LB}} \tag{25}$$

The Hagen-Poiseuille equation (2) can be used to express the velocity with the pressure gradient, resulting in equation (26). Here the diameter is replaced with the characteristic length, L, for both cases, physical and Lattice Boltzmann.

$$\left(\frac{dP}{dL}\right)_{ph} = \frac{L_{LB}^3 \cdot \rho_{LB} \cdot \mu_{ph}^2}{L_{ph}^3 \cdot \rho_{ph} \cdot \mu_{LB}^2} \left(\frac{dP}{dL}\right)_{LB} \tag{26}$$

The characteristic length can be expressed by using the resolution, see equation (23) and this results in equation (27).

$$\left(\frac{dP}{dL}\right)_{ph} = \frac{1 \cdot \rho_{LB} \cdot \mu_{ph}^2}{s^3 \cdot \rho_{ph} \cdot \mu_{LB}^2} \left(\frac{dP}{dL}\right)_{LB} \tag{27}$$

3 Theory of the Cerebral Vascular System

In this section the background regarding cerebral circulation and aneurysms is described in order to select geometries for the simulations and to interpret the results in relation to aneurysms. A description of cerebral aneurysms is covered including theory about their initiation, growth and rupture.

The cerebral circulation can be divided into arterial circulation, the transport of oxygenated blood to the brain, and venous circulation, the transport of blood from the brain [26]. As the names suggest, the arterial circulation consists of arteries and the venous circulation consists of veins. Other types of blood vessels, such as capillaries, exist as well. Capillaries are smaller in diameter and are a connection between the arteries and the veins [27].

The heart is responsible for pumping blood through the vessels and because of this the blood flow is pulsatile. The flow in the veins is not equally pulsatile as the flow in the arteries. This is due to the fact that the pulses are reduced when the blood passes through the capillaries [27].

3.1 The Circle of Willis - a Connection of Arteries

The Circle of Willis (CoW), see figure 2, is a circulatory anastomosis that consists of a number of connecting arteries, which all supply the brain and surrounding tissue with oxygenated blood. The CoW is located in the lower part of the brain and consists of the following five main arteries:

1. Internal carotid artery (ICA)
2. Anterior cerebral artery (ACA)
3. Anterior communicating artery (ACom)
4. Posterior cerebral artery (PCA)
5. Posterior communicating artery (PCom)

where 1, 2, 4 and 5 all exist on both the left and right side of the brain, whereas 3 acts as a bridge between the two sides [28]. Thanks to the CoW it does not make a great difference if one of its smaller arteries is blocked or if there is a stenosis since the other arteries may provide support in its place. Whilst the CoW remains similar in most brains, anatomical variations exist [28].

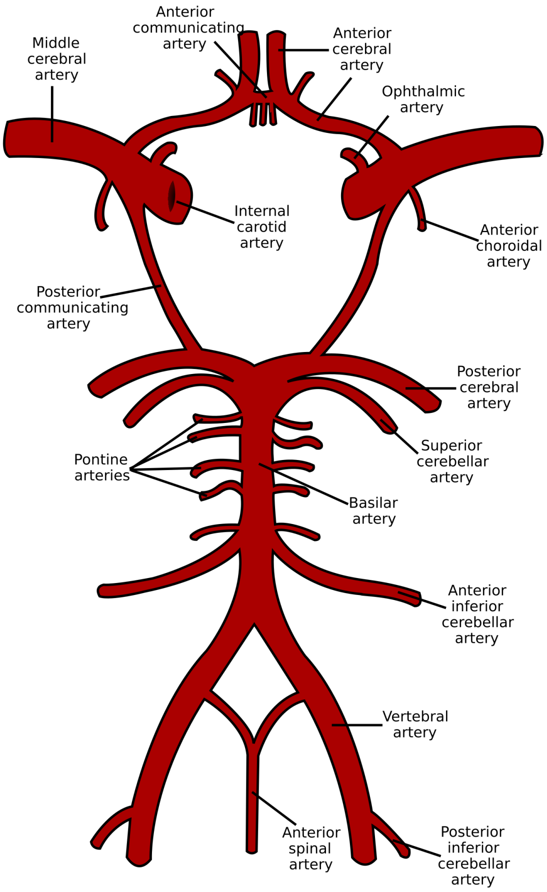

Figure 2: A general model of Circle of Willis [29]

3.2 Properties of Blood and Blood Vessels

The structure of blood vessels varies with the type of vessel, but mainly when it comes to arteries and veins there are three different layers in the blood vessel walls [30]. Starting from the outermost layer and going inwards, the first layer is the tunica adventitia, a connective tissue, with components such as collagen and nerves [27]. The second, middle layer is the tunica media and with the help of its constituent smooth muscle cells it can regulate the vessel diameter [31]. The third and innermost layer is called the tunica intima and blood is in contact with a part of this layer, the endothelium [32]. The endothelial cells that make up the endothelium fulfill different functions such as control over permeability of the blood vessel wall and inhibition of coagulation [33]. Due to its direct contact with the blood flow, the endothelium plays an essential role in the progression of aneurysms.

Plasma and cells are the two main components of blood [34]. Most of the plasma is water and a small part of it is proteins and ions [35]. Regarding the cells there exist three types with different functions in blood. Two of these are red- and white blood cells which are a part of the oxygen transport and the defence in the body, respectively [36]. The third type is platelets and they play a role in coagulation by adhering to the endothelium when injury to the blood vessel wall occurs [35].

Blood density can be used as 1050 kg/m^3 [37]. The dynamic viscosity of blood is often approximated as 0.035 Pa·s when it comes to larger arteries [38], but can range between 0.003-0.04 Pa·s [35]. Different factors affect the blood viscosity, two of them are temperature and hematocrit, the volume percentage of cells in the blood [39]. In smaller vessels the relation between hematocrit and blood viscosity is more evident [38].

Since blood flow is pulsatile, the Reynolds number for blood in intracranial arteries can vary depending on whether it is a systolic or a diastolic period of the cardiac cycle. The diameter of the blood vessel also affects the Reynolds number. One study has measured the Reynolds number in ICAs to vary from 382 to 531 during systole, and 200 to 277 during diastole [40].

The flow of blood can be approximated as a steady flow in certain cases despite its pulsatile behavior. Since the progression of aneurysms is usually linked to chronic long-term events more so than acute events, flow data that is spread over a longer time may be of greater interest than those that occur in short sudden bursts and can therefore justify a steady flow approximation [41].

Fluids may be divided into two subgroups, Newtonian and non-Newtonian fluids. The difference is that a Newtonian fluid has a constant viscosity, no matter the pressure applied to it; whereas a non-Newtonian fluid does not. The viscosity of blood also varies with the stress, and is therefore considered a non-Newtonian fluid. Blood behaves as a non-Newtonian fluid during low shear rates in smaller vessels [42]. Furthermore, shear-thinning is one characteristic that comes with blood being non-Newtonian [43]. A shear-thinning liquid implies that the viscosity decreases as stress increases. Blood can however be approximated as Newtonian [44], this can for example be applied to flow through larger vessels. It is considered reasonable due to the fact that the diameter of the vessel is much greater than the diameter of the individual cells of the fluid [45]. When blood is approximated as a Newtonian fluid the shear-thinning behavior is ignored.

3.3 Cerebral Aneurysms

A cerebral aneurysm is an enlargement of a blood vessel wall in the brain. The most common form is a saccular aneurysm, also called a berry aneurysm, which constitutes around 90% of all aneurysms [9]. As the name suggests it has a more round form and is protrusive from the wall.

It has been discovered that the size of the aneurysm depends on its location as well as the size of the location [46]. Saccular aneurysms can be divided into three different groups according to size. Small correlates to an aneurysm with a diameter less than 10 mm, a large has a diameter between 10 and 25 mm, while a giant has a diameter greater than 25 mm [9]. The arteries of the CoW are a common location for saccular aneurysms to develop, since that is where around 85% of the saccular aneurysms occur. Furthermore, saccular aneurysms are often discovered in the vicinity of the CoW but also where arteries bifurcate [47, 48]. The most common location for cerebral aneurysms is ACom which is located in the frontal area of the CoW [49], see figure 2. ACom is quite a small artery that acts as a connection between the left and right ACA to stabilize the blood flow [50]. The length of ACom is approximately 4 mm [51] even though some anatomical variations are common. The size of a saccular aneurysm located in ACom varies but usually has a diameter between 3-6 mm whereas an aneurysm located in the ICA may have a larger diameter ($\sim$ 6-8 mm) due to the size of the artery [46].

In the general human population up to 3% have a cerebral aneurysm which has not ruptured, and several aneurysms can be present at once which is the case for 20-30% of the patients [52]. Headaches and seizures are two examples of symptoms from unruptured aneurysms, however they do not always show symptoms which is often the case with smaller aneurysms [48]. Today cerebral aneurysms are detected more easily due to progress in imaging techniques used within medicine, where magnetic resonance imaging and computed tomography are two examples of techniques [4].

When an aneurysm ruptures it can cause subarachnoid hemorrhage (SAH), which is a type of brain bleed and therefore a form of stroke [53]. While trauma is generally the leading cause of SAH [54], a ruptured intracranial aneurysm is the most common non-traumatic cause of SAH [37].

Subarachnoid hemorrhage is one of the most severe consequences of a rupture and has a high fatality rate. Around 30-40% of cases with a SAH are fatal [48] and many of the patients with SAH are at a young age [47]. Small aneurysms have a rupture risk of about 0.7% every year [55]. Rupture does not occur for the majority of aneurysms [47].

Two surgical treatments of aneurysms are clipping and coiling [35]. When using clipping the blood circulation is cut off from the aneurysm with a clip to achieve a more normal circulation. Coiling entails the insertion of a metal coil in the aneurysm, which will lead to clotting of the blood around the coil and therefore prevents blood from flowing in the aneurysm.

The progression of aneurysms is still not fully understood and there are different suggestions for the reasons behind it. One parameter that suggests a strong connection between hemodynamics and intracranial aneurysm pathogenesis is wall shear stress (WSS). The wall shear stress is the tangential, frictional force on the blood vessel walls. It is an important parameter because it affects the endothelial cells and their functions [6].

3.3.1 Initiation of Cerebral Aneurysms

The initiation of intracranial aneurysms has been shown to be connected with high WSS and a mechanism called endothelium-mediated mechanotransduction [3, 56]. The mechanism involves endothelial cells sensing WSS and subsequently acting on the mechanical signals from the WSS by transducing them into biochemical signals. These biochemical signals can in turn initiate vascular remodeling of the blood vessel in order to restore and maintain homeostasis, a level of biological stability, that the mechanical stress has affected [57]. When blood vessel walls are exposed to chronically elevated WSS [58], see figure 3a, the current homeostasis gets disrupted. This in turn triggers the above mentioned endothelium-mediated mechanotransduction to expand the blood vessel wall outwards. As the affected area of the blood vessel wall undergoes expansion, the conditions begin to return to baseline WSS levels in order to restore homeostasis. If homeostasis is not restored in time, the outward expansion continues and becomes a destructive remodeling of the blood vessel wall which leads to an initiated aneurysm, see figure 3b.

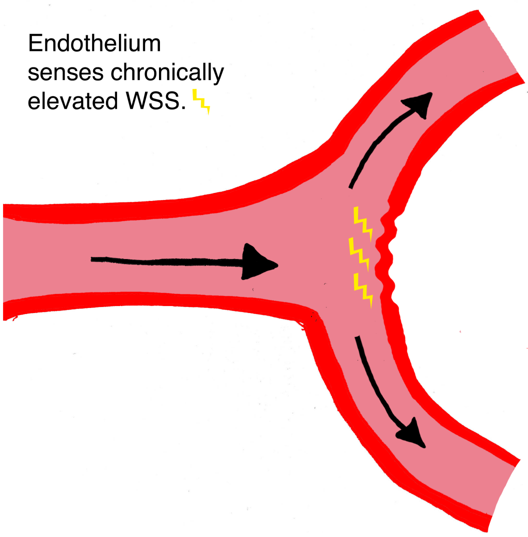

(a) Blood flow affecting endothelial cells on blood vessel wall at a high WSS location

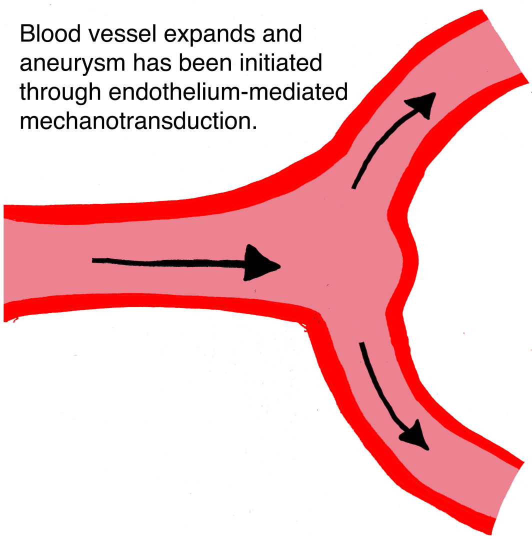

(b) Beginning of destructive remodeling of blood vessel wall

Figure 3: The progress of aneurysm initiation on a blood vessel bifurcation (authors' own images)

3.3.2 Growth and Rupture of Cerebral Aneurysms

While the initiation of intracranial aneurysms has been strongly linked to high WSS, the continued growth and rupture of aneurysms have on the other hand been connected to both high and low WSS [56]. Depending on the geometry of the vasculature near the initiated aneurysm, two different general flow characteristics have been shown to cause two different mechanisms that can trigger the growth and rupture of aneurysms.

The first is when the blood flow into the initiated aneurysm is low and has a slow recirculation inside the aneurysm [6]. The flow is characterized by low WSS. Blood stagnation occurs in the dome as the low WSS along the endothelial surfaces causes the blood cells to coagulate. This elicits an inflammatory response in the endothelium which causes the bulge to expand further and eventually rupture, see figure 4a.

The second case that points towards growth and rupture of aneurysms is if there is a persisting impinging flow into the aneurysm after its formation [59]. The impinging flow is characterized by a high WSS that stays prevalent inside the aneurysm. This activates a mechanism called mural-cell-mediated destructive remodeling, which can also cause the aneurysm to grow and rupture, see figure 4b.

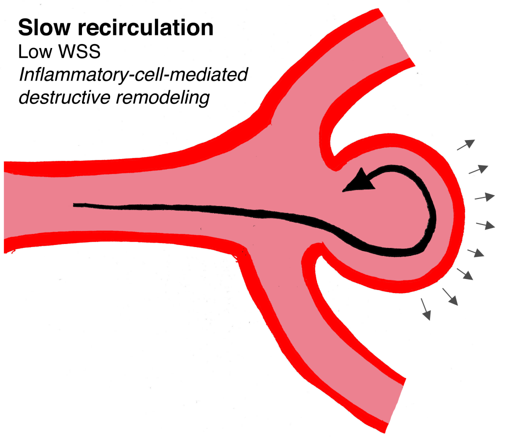

(a) Slow recirculating flow into an aneurysm

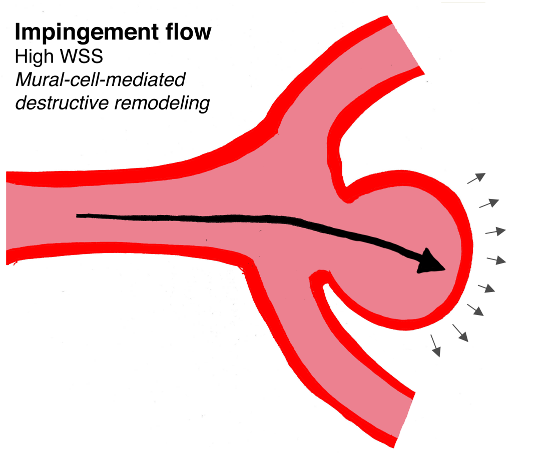

(b) Impinging flow into an aneurysm

Figure 4: Two flow characteristics that elicit aneurysm growth and rupture (authors' own images)

4 Method

This chapter describes the processes that were performed in order to obtain the forthcoming results. It starts with the acquisition and reconstruction of geometries of the human vascular system from images of MRI scans, followed by the implementation of the Lattice Boltzmann method (LBM) in the MATLAB code. It concludes with the validation of said MATLAB code in regards to the LBM and shear stress calculations.

4.1 Image Reconstruction

The images of the two human brains, denoted BG0001 and BH0027, were reconstructed into three-dimensional volumetric data in MATLAB. This was done by adding the DICOM images together, in order. The DICOM images were taken from the MRI scans of the aforementioned brains. The vascular system was afterwards singled out by extraction of data with different manually chosen threshold values depending on the noise surrounding the blood vessels. Given the volumetric data of the brain, initially in low resolution, it could be visualized by means of an isometric surface projection in a 3D plot, and regions of interest in the vascular system could thereafter be identified.

As mentioned in section 1.2, the CoW was chosen as the general region of interest in the brain. After specific blood vessels in the CoW had been identified as interesting from the 3D plot, a MATLAB script was run with specified coordinates of the brain and now with higher resolution which resulted in the attainment of detailed geometries of the chosen vascular areas. With higher resolution comes a greater number of mesh elements. While choosing a high enough resolution for the geometries, approximately 15 million mesh elements per geometry was the aim. This led to simulation times of approximately four hours to one day which was considered fitting within the time frame of the project. The in- and outlets of the blood vessels in the selected regions required buffers, additional volume outside of the geometry, which use periodic boundary conditions in all directions. The buffers need to be of appropriate dimension so that the fluid can resume a flow of unaffected nature when entering and exiting a specific geometry.

4.2 Choice of Geometries

After reconstructing the images of BG0001 and BH0027 it was notable that the two brains had geometrical differences in regards to cardiovascular structure. The CoW was located in the two brains, which can be seen in figures 5 and 6.

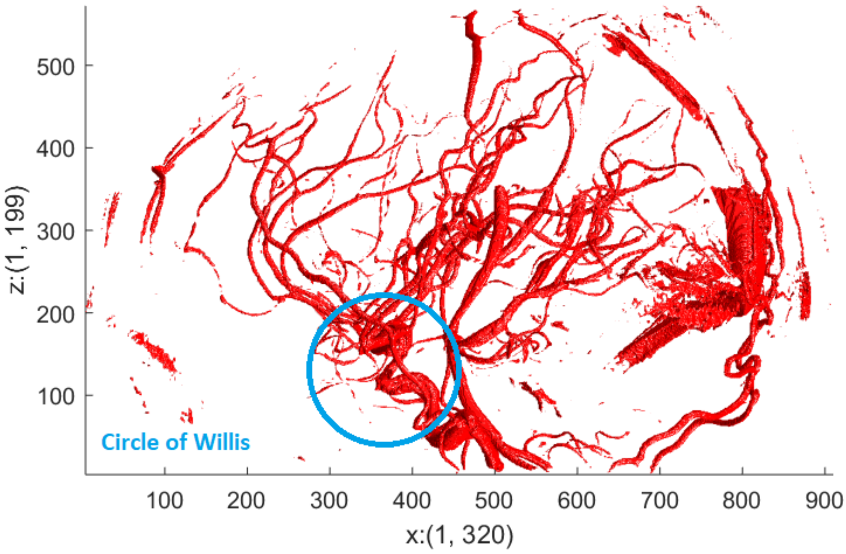

Figure 5: BG0001 displayed from the side showing the location of CoW (authors' own image)

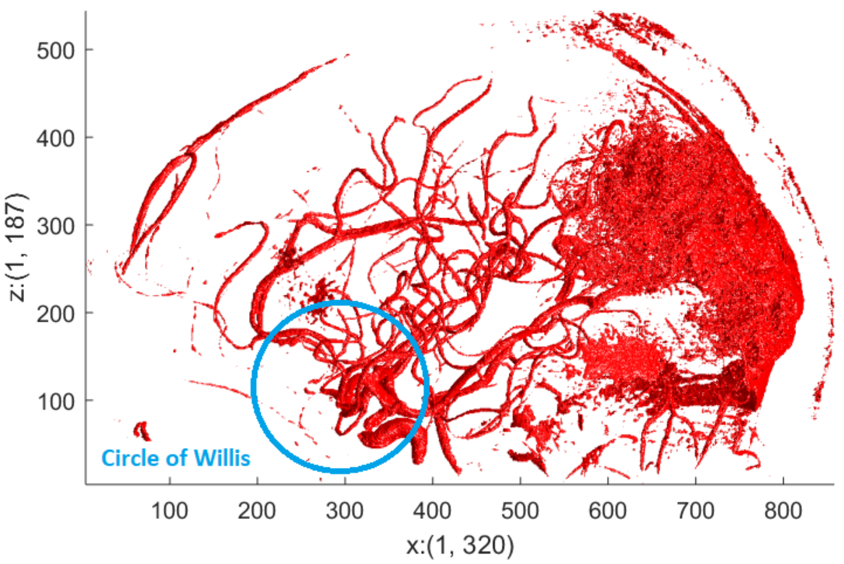

Figure 6: BH0027 displayed from the side showing the location of CoW (authors' own image)

When it came to choosing specific regions of interest in the CoW, four geometries were chosen in BG0001 while three were chosen in BH0027. These can all be seen in figures 7 and 8. When BG0001 and BH0027 were compared with one another it was possible to find a couple of common extractable geometries, namely P1 and ACom. Figure 7a displays the artery called P1 in BG0001. The flow entering P1 originates from the vertebral arteries, the major arteries of the neck. The vertebral artery supplies the CoW with oxygenated blood through the basilar artery. The fluid flow in P1 in BG0001 is therefore in negative y-direction.

Furthermore, figure 7b represents a curvature in BG0001 which is located near the ICA on the right side of the brain (Rt ICA). The flow through the curvature at the Rt ICA comes from P1 and continues through the ICA towards ACA and ACom. When simulating the direction of the stream through the curvature at the Rt ICA the fluid was pushed in a positive z-direction. The curvature was chosen since it contributed to a larger variety of differently shaped vascular geometries to use for simulations.

Another selected geometry was a bifurcation located by the Rt ICA, near the curvature, see figure 7c. Here the blood flow originates from the ICA and is divided into two branches, one of the streams continues towards ACA and ACom whilst the other continues through the middle cerebral artery. This implies that the fluid flows in a negative y-direction. The bifurcation in BG0001 was chosen because of the likelihood of aneurysms developing at bifurcations.

Figure 7d displays a reconstructed image of ACom. In the anterior communicating artery the fluid flows through ACA. In this geometry it was natural to push the flow in a positive x-direction. As mentioned in section 3.3 ACom is a small artery which connects the ACA on the left and right side and is present to stabilize the blood flow through the CoW.

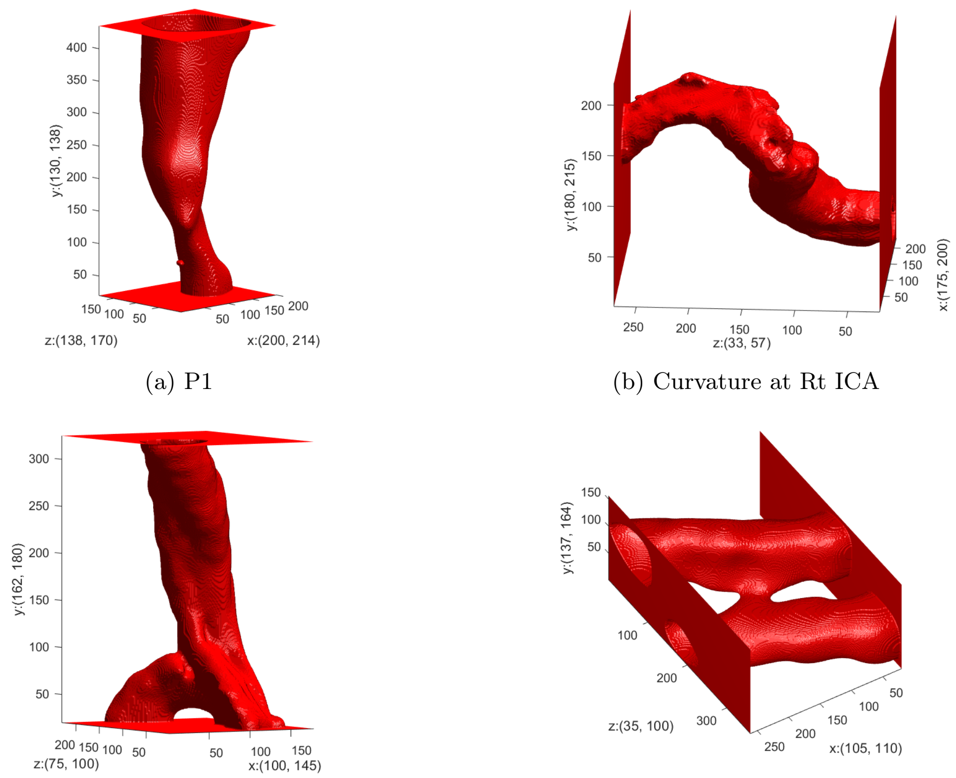

(a) P1

(b) Curvature at Rt ICA

(c) Bifurcation at Rt ICA

(d) ACom

Figure 7: Four different geometries in CoW in BG0001 (authors' own images)

Figure 8a shows the reconstructed image of P1 in BH0027. The artery could be found in both BG0001 as well as BH0027. The fluid flow through P1 was pushed in a positive y-direction. Figure 8b displays the Rt ICA in BH0027. This artery was selected in order to compare with the geometries, in the same area, received from BG0001. In the same way as in BG0001 the fluid origins from the top of the basilar artery and P1. The direction of the fluid was naturally chosen in a negative x-direction. Lastly, figure 8c represents ACom in BH0027. The flow through the geometry was chosen in a negative x-direction.

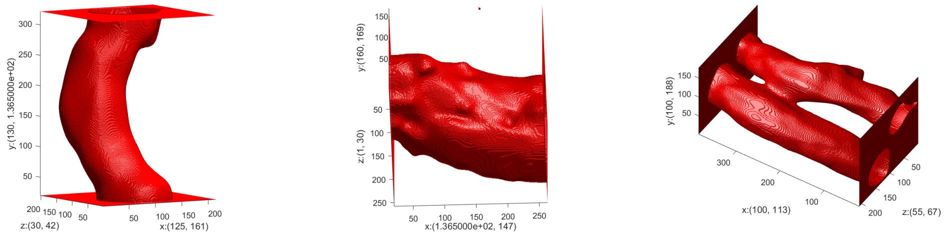

(a) P1 (b) Rt ICA (c) ACom

Figure 8: Three different geometries in CoW in BH0027 (authors' own images)

Figures 9 and 10 represent the full images of BG0001 and BH0027, where the selected geometries are marked.

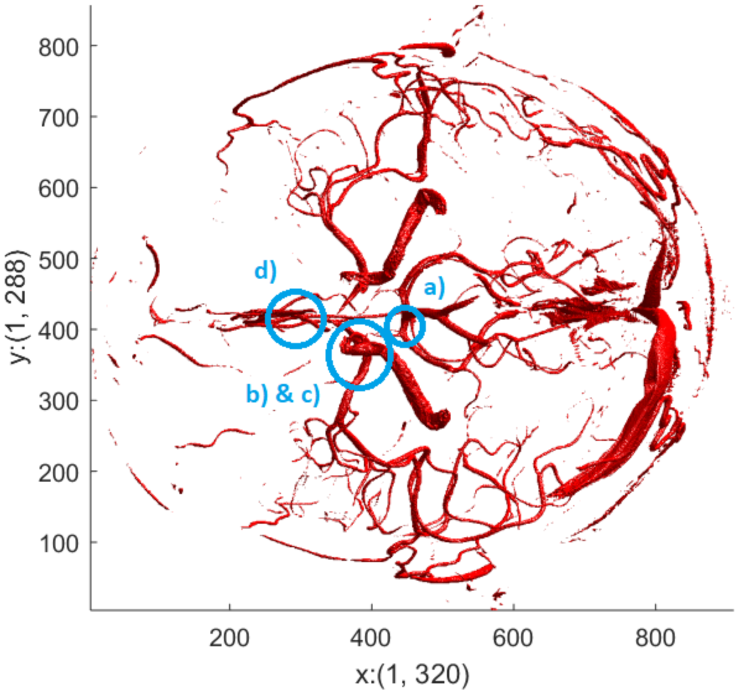

Figure 9: BG0001 displayed from below showing the selected geometries (authors' own image)

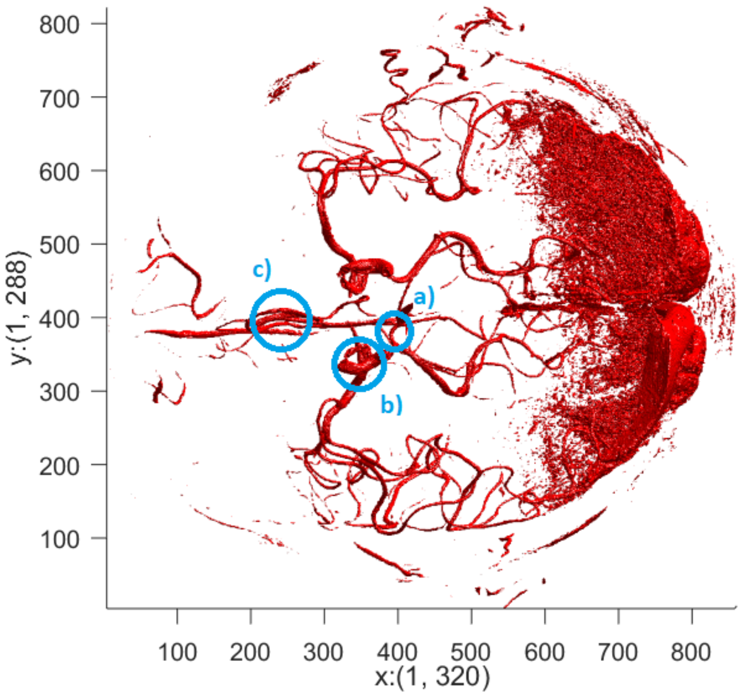

Figure 10: BH0027 displayed from below showing the selected geometries (authors' own image)

The specifications for the different chosen geometries can be seen in table 1. The length and diameter are the real dimensions of the blood vessels. The ratios are regarding the length of the geometry divided by the buffer length and the geometry length divided by the diameter.

Table 1: Specifications and ratios for geometries

Geometry	***Real Length [mm]***	***Real Diameter [mm]***	***Ratio 1,*** $\frac{geometry\ length}{buffer\ length}$	***Ratio 2,*** $\frac{geometry\ length}{distance\ between\ plates}$	***Number of mesh elements***	***Pressure gradient [Pa]***
P1 (BG0001)	5.8	1.6	10.8	3.7	$16.5 \cdot 10^6$	540
Curvature at Rt ICA (BG0001)	20.1	3.7	8.1	5.4	$14.9 \cdot 10^6$	58
Bifurcation at Rt ICA (BG0001)	11.8	3.7	7.2	3.2	$14.1 \cdot 10^6$	104
ACom (BG0001)	3.7	1.2	6.0	3.2	$15.7 \cdot 10^6$	896
P1 (BH0027)	4.4	1.7	7.6	2.5	$14.7 \cdot 10^6$	504
Rt ICA (BH0027)	8.1	3.9	7.2	2.1	$12.6 \cdot 10^6$	22
ACom (BH0027)	8.7	1.7	9.1	5.2	$14.2 \cdot 10^6$	290

4.3 Flow Simulation

The Lattice Boltzmann method described in section 2.4 was implemented in MATLAB from an initial template provided by the supervisor. For a start, smaller simulations were done with limited computational power, which is enough for smaller, low resolution models and for simple geometries used in validation of the code. For larger simulations of more complicated geometries with high resolution, simulations were done with the PC-cluster 'Hebbe' available at Chalmers University of Technology.

4.3.1 Limitations Regarding Simulations

In order to simulate the blood flow, several approximations were done. Firstly, blood was approximated as a Newtonian fluid. As mentioned in section 3.2, it is reasonable to approximate that blood has a constant viscosity since the non-Newtonian effects are usually negligible. Secondly, the geometries were assumed to be rigid, therefore changes in the blood vessel structure and the wall was not taken into consideration. In addition, low Reynolds numbers were used because of limitations in computational power and the long accompanying simulation times that it would require. Therefore a Reynolds number of 0.03 was used for the simulations, even though the usual Reynolds numbers lie around 100-500 for vessels in the CoW. This means that the flow was approximated as Stokes flow with low velocities. Lastly, the flow was assumed to be steady and laminar, which implies no pulses.

4.3.2 Implementation

Although the initial script for computing Lattice Boltzmann steady state velocity solutions was provided by the supervisor, several alterations have since been made in order to improve the speed at which the code runs, and the memory usage. Here follows an abbreviated explanation of the general idea behind the implementation of the code.

Two steps that are central to the Lattice Boltzmann algorithm are the propagation or streaming step and the collision step based on an equilibrium distribution. The propagation step is generally described according to equation (28) which describes a versorwise movement of the probability density function components amongst the nodes. Generally speaking, this can be reduced to a simple index mapping, or in other words changing which index maps to which versor node value. This also handles non-multireflection bounceback boundary conditions as described in equation (29), which occur in the border between fluid and solid geometry. The index mapping is the currently implemented usage of this step, where the map is generated from the desired geometry before the iterative loop is run.

$$f_a(i,j,k) = f_a(i+\mathbf{e}_{x,a}, j+\mathbf{e}_{y,a}, k+\mathbf{e}_{z,a}) \tag{28}$$

$$f_{\text{Opposite of } a}(i,j,k) = f_a(i,j,k) \tag{29}$$

The collision step in MRT-models are handled according to equation (14), with the caveat that in the current implementation, the S matrix is instead a versorwise scalar, due to being faster, and allowing for future implementations of a non-Newtonian variant, as well as the addition of a driving force F according to equation (30).

$$F = -\left(1 - \frac{\mathbf{S}}{2}\right)\mathbf{MW}\sum_i \left(3e_{i,.} - 3U_i + 9e_{i,.}^2 U_i\right)\nabla P \tag{30}$$

For the implementation of the equilibrium density function f_{eq} the velocity needs to be calculated. This is done according to equation (31) with the modifications that the code skips all j where $e_{i,j} = 0$, since that would be adding a term to the sum which would be multiplied by zero, hence having a zero contribution to the sum.

$$U_i = \sum_j f_j e_{i,j} + \frac{1}{2}\frac{\partial P}{\partial i} \tag{31}$$

The equilibrium calculation is based upon equation (12), but seeing as the **EQ** matrix is sparse, each row is calculated manually in the code, for example $f_{eq,1} = \rho$ and $f_{eq,2} = -11\rho + \frac{19}{\rho_g}\sum_i U_i$, which yields a faster iteration time.

To further speed up iteration time, all solid nodes are excluded from the calculation prior to the iterative loop start, so that only the fluid nodes, which are the only ones that change, are actually passed through the necessary operations.

Furthermore, some values were needed in the preparation of the simulation, these are given here to enable the possibility to recreate the method. First the pressure gradient for the simulations was calculated by using the expected Reynolds number mentioned previously and the equations for Reynolds number and Hagen-Poiseuille are shown in equations (1) and (2). The characteristic length in the equations was used as the geometry volume divided by the surface area. Density and kinematic viscosity was used as 1 and 1/6 in LB-units, respectively, for the simulations. The residual, a measure of difference, in each iteration was based on a comparison of the Reynolds number between the present and the former iteration. To determine the final convergence of the simulation a tolerance was decided to 10^{-6}. The shear stress was calculated through implementation of the equations under section 2.5. The shear stress values were converted to SI units from LB-units by using the equations described in section 2.6. The dynamic viscosity was used as 0.035 Pa·s and the density as 1050 kg/m^3. The pressure gradient was also converted to SI units from LB-units after the simulations.

4.3.3 Cluster Hebbe

For larger simulations, usually in excess of 15 million nodes, there was a need for more computing power. To achieve this, simulations were run on the centOS cluster Hebbe at Chalmers University of Technology, with minor modifications to the simulation code to ease the creation of the necessary batch scripts to run it.

4.3.4 Insertion of Aneurysm

Since aneurysms have been shown to initiate on areas of high WSS, the corresponding maximum or high WSS areas were located from the simulations of the chosen geometries. In the located area an aneurysm was inserted through a construction of a sphere in MATLAB, therefore the general aneurysm shape was approximated to be a sphere. The diameters used for the spherical aneurysms can be seen in table 2. The size of the aneurysm was chosen with the information gathered from section 3.3 as a basis and to test a few different sizes. Simulations were run in the cluster for the geometries with constructed aneurysms and the same fixed pressure gradient was used as in the case without aneurysm. The shear stress was then calculated.

Table 2: Diameters of inserted aneurysms

Geometry	***Aneurysm diameter [mm]***
P1 (BG0001)	0.8
Curvature at Rt ICA (BG0001)	3
Bifurcation at Rt ICA (BG0001)	3
ACom (BG0001)	1.2
P1 (BH0027)	1.6
Rt ICA (BH0027)	1.6
ACom (BH0027)	2.4

4.4 Validation of Flow Calculations

In order to guarantee correct implementation of the MATLAB code regarding the LBM and shear stress, different geometries were tested and compared to theoretical velocity profiles from literature. In the following two sections the completed validation of two- and three-dimensional fluid flow is presented.

4.4.1 Two-Dimensional Validation

For the 2D validation a geometry with two parallel plates was constructed in MATLAB, initially excluding buffers, with a length of 101 Lattice Boltzmann nodes (LB-nodes) and a distance of 21 LB-nodes between the plates. A simulation was performed to compute the velocities, and the velocity profile from the simulation and the literature, see equation (5), was compared. The shear stress was computed and the shear stress profile based on the simulations and the literature, see equation (7), was compared. In the equations the parameters were used in LB-units. This was also done for a plate length of 151 LB-nodes and a plate length of 201 LB-nodes, both cases with a diameter of 21 LB-nodes. These cases can be seen in table 3 with the corresponding pressure gradient.

The chosen geometries from the vascular system required a buffer at both ends of the geometry to enable the flow boundary conditions to implement accordingly. Therefore, different two-dimensional cases of varying ratios between the length of the plates and the buffer length was tested, see table 3. Cases with different ratios between the length of the plates and the distance between the plates were also tested. The first case with buffer size 20 corresponds to a buffer length of 40 since it was added to both the inlet and outlet of the geometry. The same computations and comparisons as previously described were made, using the same equations as the first case of the two parallel plates.

Table 3: The tested cases for flow between parallel plates

Plate length [LB]	***Buffer length [LB]***	***Distance between plates [LB]***	***Ratio 1,*** $\frac{plate\ length}{buffer\ length}$	***Ratio 2,*** $\frac{plate\ length}{distance\ between\ plates}$	***Pressure gradient [LB]***
101	0	21	-	4.8	$2.3{\cdot}10^{-5}$
101	40	21	2.5	4.8	$2.3{\cdot}10^{-5}$
101	60	21	1.7	4.8	$2.3{\cdot}10^{-5}$
101	80	21	1.3	4.8	$2.3{\cdot}10^{-5}$
151	0	21	-	7.2	$2.3{\cdot}10^{-5}$
151	40	21	3.8	7.2	$2.3{\cdot}10^{-5}$
151	60	21	2.5	7.2	$2.3{\cdot}10^{-5}$
151	80	21	1.9	7.2	$2.3{\cdot}10^{-5}$
201	0	21	-	9.6	$2.3{\cdot}10^{-5}$
201	40	21	5.0	9.6	$2.3{\cdot}10^{-5}$
201	60	21	3.4	9.6	$2.3{\cdot}10^{-5}$
201	80	21	2.5	9.6	$2.3{\cdot}10^{-5}$
101	40	41	2.5	2.5	$3.1{\cdot}10^{-6}$
201	40	41	5.0	5.0	$3.1{\cdot}10^{-6}$

Figure 11 illustrates the impact of the different buffer lengths, 0, 40, 60 and 80, compared to the theoretical velocity and shear stress. The velocity profiles and shear stress profiles are constructed for a cross section for the middle of the plate length when regarding a plate length of 101 and a distance between plates of 21. The maximum velocity is larger for an increasing buffer length. The slope of the shear stress profiles is increasing with a higher value of buffer length. For all cases the shape of the profiles are equal to the shape of the theoretical profiles. It can be seen that the points with zero velocity for the simulated profiles are outside of the plate. This is because when constructing the geometry, the plate is between two points and therefore the velocity at points right before and after the plate was calculated.

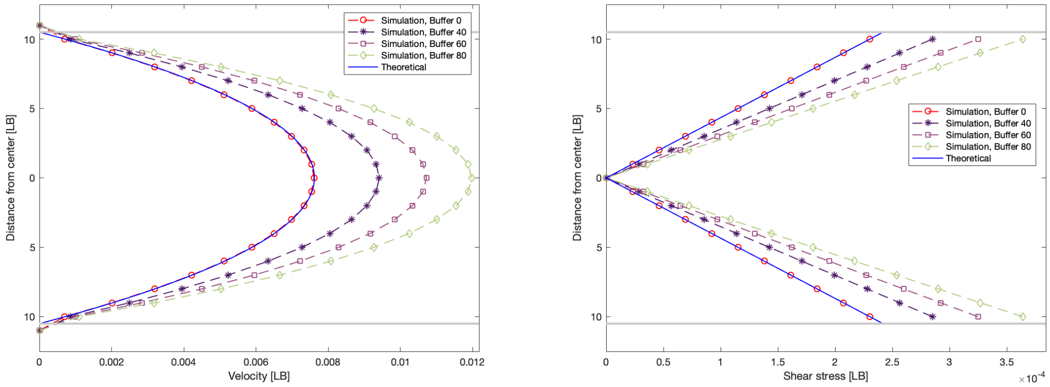

(a) Velocity profiles (b) Shear stress profiles

Figure 11: Velocity profiles and shear stress profiles between two parallel plates with different buffer lengths, a plate length of 101 and a distance between plates as 21 LB-nodes (authors' own images)

The magnitude of the velocity profiles varies for different cross sections of the plate length in the two dimensional-case, but the profile is parabolic for all cases. This can be seen in figure 12 for a cross section in the inlet, the middle of the plate length and the outlet. The magnitude varies because the inlet and outlet are affected by the buffer.

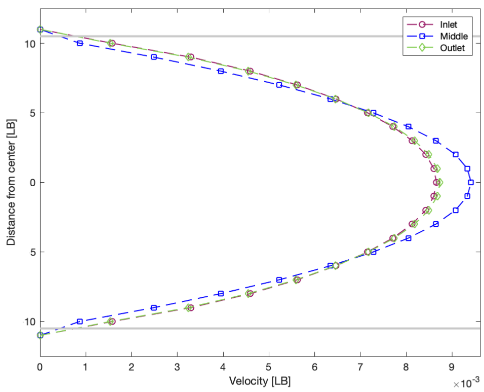

Figure 12: Velocity profiles between two parallel plates for different cross sections when using buffer length 40, plate length 101 and distance between plates as 21 LB-nodes (authors' own image)

Geometries regarding flow between two parallel plates were constructed based on the ratios for the chosen geometries in the vascular system. The geometries and the ratios can be seen in table 4 with the corresponding pressure gradient for the two-dimensional case. Simulations were run on these two-dimensional geometries and velocity profiles were created and compared to the theoretical velocity profiles based on equation (5).

Table 4: Ratios and pressure gradient for the two-dimensional cases corresponding to the chosen geometries

Corresponding geometry	***Ratio 1,*** $\frac{plate\ length}{buffer\ length}$	***Ratio 2,*** $\frac{plate\ length}{distance\ between\ plates}$	***Pressure gradient, [LB]***
P1 (BH0027)	7.6	2.5	$1.20 \cdot 10^{-7}$
Rt ICA (BH0027)	7.2	2.1	$8.30 \cdot 10^{-8}$
ACom (BH0027)	9.1	5.2	$5.96 \cdot 10^{-7}$
P1 (BG0001)	10.8	3.7	$1.33 \cdot 10^{-7}$
RtICA branching (BG0001)	7.2	3.2	$2.49 \cdot 10^{-7}$
ACom (BG0001)	6.0	3.2	$5.06 \cdot 10^{-7}$
Curvature (BG0001)	8.1	5.4	$9.40 \cdot 10^{-7}$

Velocity profiles for the two-dimensional case with a ratio corresponding to the geometry P1 in BG0001 can be seen in figure 13a. Both the velocity profile based upon the simulation and the literature can be seen. Furthermore, the same profiles based on the ratios for P1 in BH0027 can be seen in figure 13b. In both figures there is a small difference in the magnitude between the velocity profiles, but all profiles are parabolic. In appendix A similar results can be seen for the other ratios corresponding to the chosen geometries, see table 1.

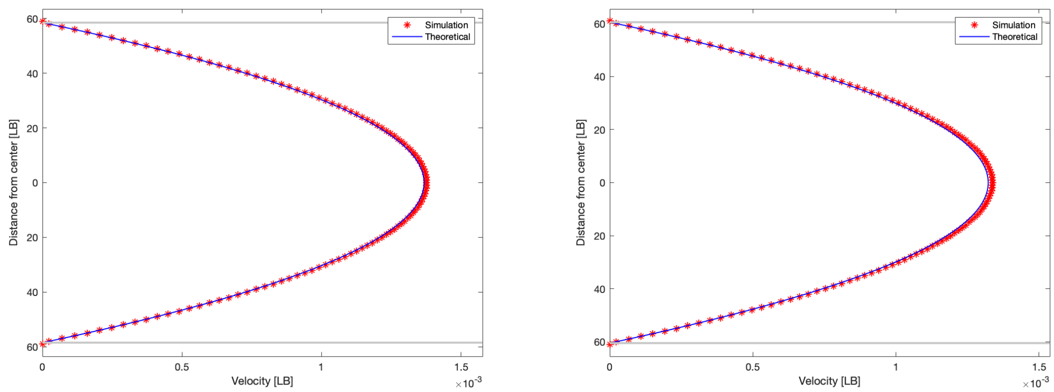

(a) P1 - BG0001

(b) P1 - BH0027

Figure 13: Velocity profiles between two parallel plates with ratios corresponding to chosen geometries for a cross section in the middle of the length (authors' own images)

4.4.2 Three-Dimensional Validation

For validation of velocity and shear stress regarding three-dimensional geometries, straight pipes were constructed in MATLAB. The size specifications of the pipes are given in table 5. In this case of validation all geometries were simulated without a buffer, because the buffer effects were evaluated from the two-dimensional validation. The specifications of the three pipes were chosen to be similar to three cases of geometries corresponding to arteries in the brain. For each of the differently sized pipes a simulation was performed and the shear stress computed. The velocity and shear stress profiles from simulation and literature was compared. The theoretical velocity profile and shear stress profile were based on equation (3) and (4), respectively and given in figure 14. For the equations the parameters were used in LB-units.

Table 5: The tested cases for flow in a three-dimensional pipe

Length [LB]	*Diameter [LB]*	*Pressure gradient [LB]*
401	101	$3.4 \cdot 10^{-6}$
301	101	$3.4 \cdot 10^{-6}$
281	141	$1.3 \cdot 10^{-6}$

In figure 14 it is possible to see a difference in the velocity profile, especially close to the wall. This is due to the uneven shape of the geometry used in simulation, see figure 15. Here the uneven geometry causes a greater contact surface compared to a perfect cylinder and the velocity is therefore reduced compared to the theoretical case. This affects the shear stress and is seen in figure 14b. In the middle of the pipe the shear stress aligns with the theoretical values, but close to the wall a decrease occurs. The two remaining pipes from table 5 are presented in appendix A.2.

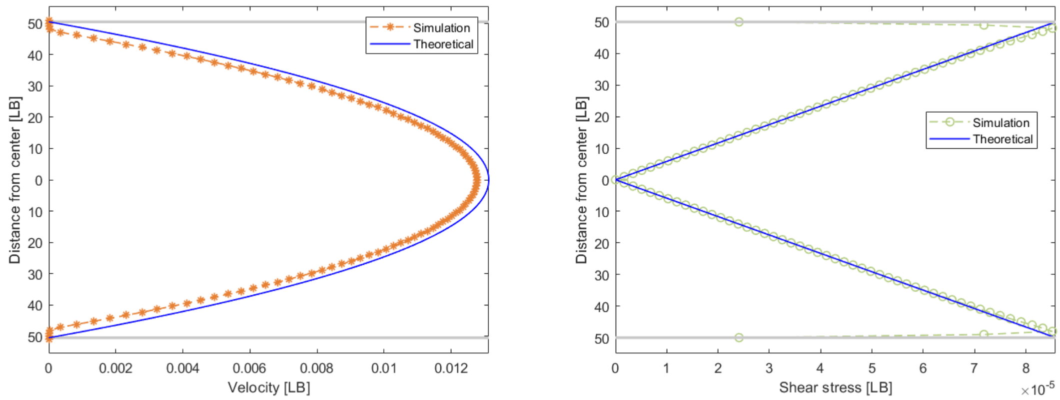

(a) Velocity profile

(b) Shear stress profile

Figure 14: Velocity- and shear stress profile in a three-dimensional pipe without buffer, pipe length 401 and diameter 101 LB-nodes (authors' own images)

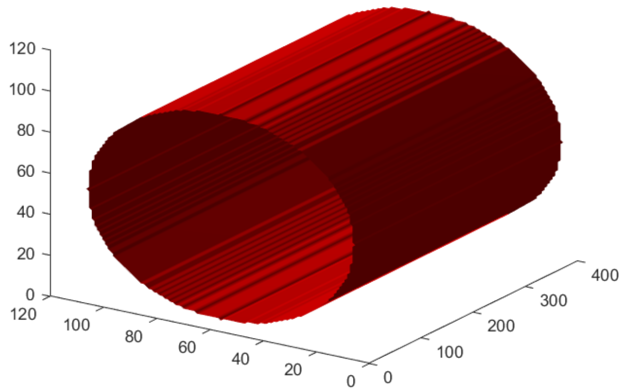

Figure 15: Geometry of the simulated pipe treated above, pipe length 401 and diameter 101 LB-nodes (authors' own image)

4.4.3 Conclusions of Validation

The validation made in the previous sections clearly shows how the buffer size affects the simulated velocity and therefore the shear stress in extension. This motivated the decision of a total buffer length of 40 for all the simulated geometries corresponding to arteries in CoW. With this the deviation from the theoretical velocities was low and the fluid had a chance to resume geometry-independent flow inside of the buffer. Furthermore, the validation with the ratios defined correspondingly to geometries showed little to no difference to the theoretical velocity.

Based upon the validation, the methodology was considered to be applicable for further simulations regarding geometries in the vascular system. This because the general shapes of the profiles are corresponding to the theoretical. An effect from the geometry and the buffer can be expected as explained.

5 Results

The results for the chosen geometries are represented with figures of the WSS, both without and with aneurysm. The figures also clarify where the aneurysms are placed. Figures that display the mean shear stress in the flow direction of the geometry and cross sections of the geometry with the shear stress are also shown in the result. The sizes of the aneurysms can be seen in table 2, section 4.3.4.

5.1 Comparison of Shear Stress between Geometries with and without a Constructed Aneurysm

Figure 16 shows the difference in WSS between the two cases without and with aneurysm in 16a and 16b respectively. The aneurysm was inserted at a location of high WSS. The maximum WSS in this geometry was found to be 0.2 Pa. Note that in corresponding figures later in the section the maximum value of the colorbar will be in the range of 0.12 to 0.86 Pa to display the locally varying magnitudes of each blood vessel more clearly.

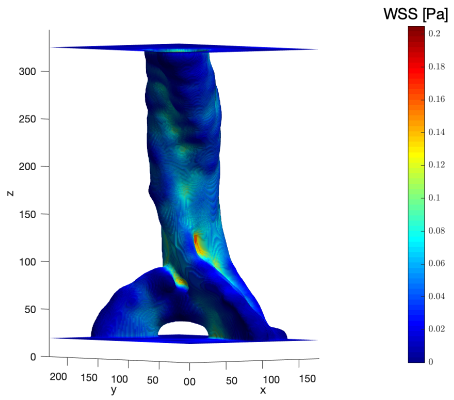

(a) Without aneurysm

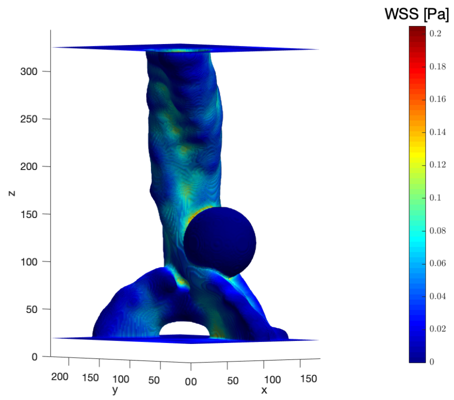

(b) With aneurysm

Figure 16: Wall shear stress for bifurcation at Rt ICA in BG0001, without and with an aneurysm (authors' own images)

In figure 17 it is possible to see the mean shear stress in the artery, calculated in the direction of the flow. The black and blue curves describe the shear stress in Rt ICA bifurcation with and without aneurysm. The orange lines represent the cross-sectional area of the artery along the flow direction. The dashed line indicates the cross-sectional area of the artery with an aneurysm inserted. Here it is possible to relate the varying mean shear stress to changes in area of the geometry. In general there is lower mean shear stress where the area is greater and the mean shear stress rises for more narrow parts of the artery. Globally the mean shear stress rises with an inserted aneurysm, with a smaller difference where the area is larger and a maximum difference after the aneurysm where the area of the geometry is low.

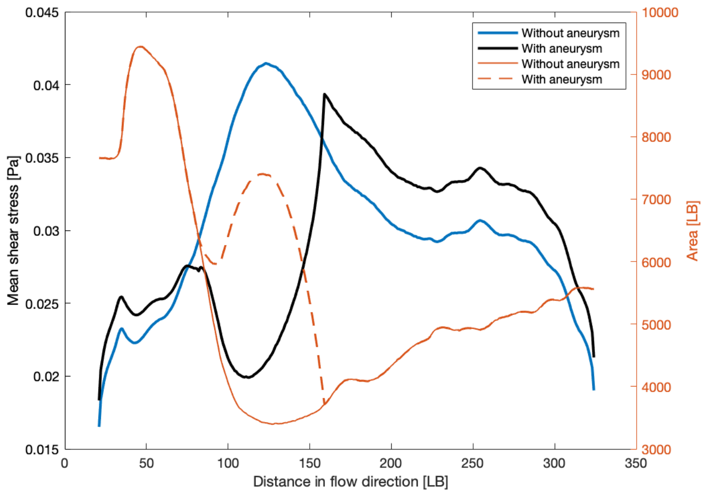

Figure 17: Mean shear stress for bifurcation at Rt ICA in BG0001 without an aneurysm and with an aneurysm with Reynolds number 0.277 and 0.292 respectively and one LB area unit is $1.502 \cdot 10^{-9}$ m^2. Average mean shear stress increase is 10% (authors' own image)

The WSS for Rt ICA curvature can be seen in figure 18 both with and without an aneurysm. The aneurysm was inserted in the region of higher WSS which is seen to be located in the part with lower diameter.

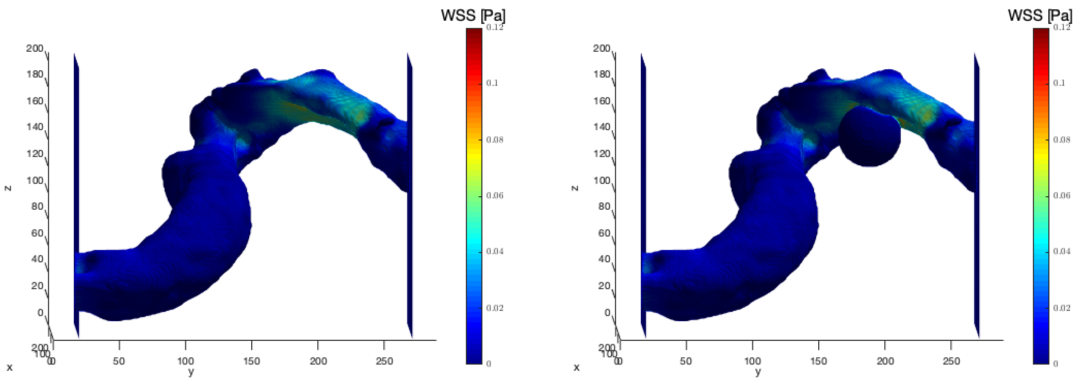

(a) Without aneurysm

(b) With aneurysm

Figure 18: Wall shear stress for curvature at Rt ICA in BG0001, without and with an aneurysm (authors' own images)

The mean shear stress for Rt ICA curvature in the flow direction is higher with lower area for the case of no aneurysm, see figure 19, which is seen in figure 18. The mean shear stress decreased with an increase in area and also decreased locally where the aneurysm was inserted. It also corresponds to an increase of area. The mean shear stress increased globally with the insertion of an aneurysm.

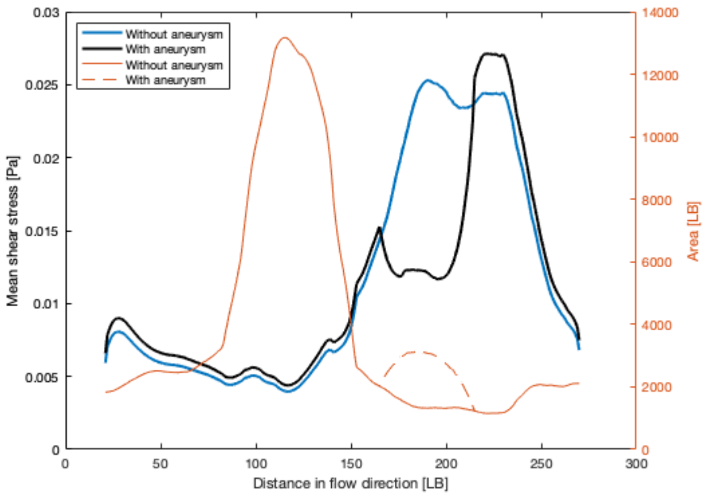

Figure 19: Mean shear stress for curvature at Rt ICA in BG0001 without an aneurysm and with an aneurysm with Reynolds number 0.0471 and 0.0512 respectively and one LB area unit is $3.844 \cdot 10^{-9}$ m^2. Average mean shear stress increase is 10% (authors' own image)

The WSS of P1 in BG0001 is shown in figure 20, here the WSS is significantly higher than the two previous treated arteries, now with a maximum WSS of around 0.69 in the case with an inserted aneurysm.

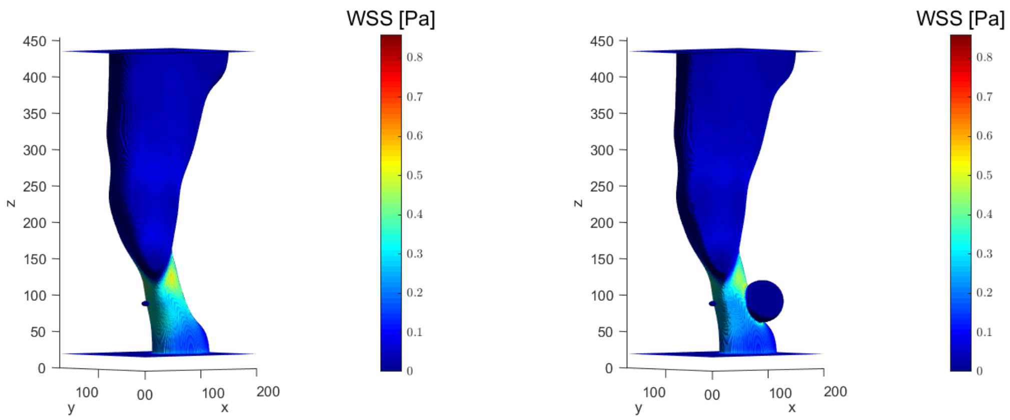

(a) Without aneurysm

(b) With aneurysm

Figure 20: Wall shear stress for P1 in BG0001, without and with an aneurysm (authors' own images)

In figure 21 there is little to no difference in mean shear stress along the flow direction. The increase in WSS directly after the aneurysm, seen in figure 20, does not show in this plot since the mean of the shear stress is calculated.

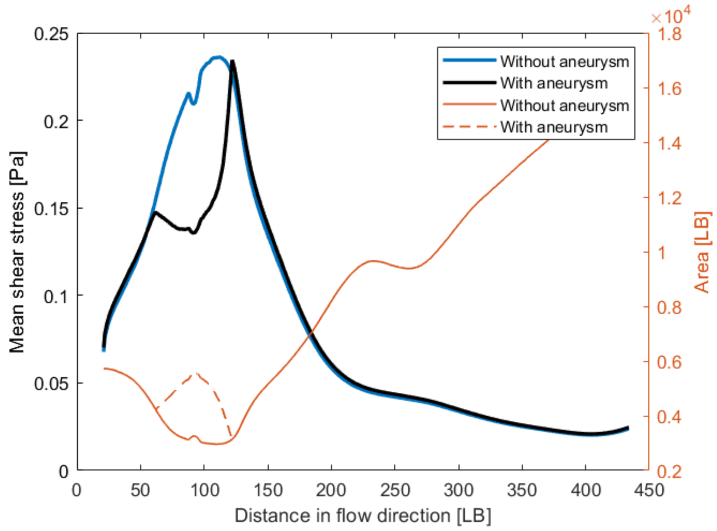

Figure 21: Mean shear stress for P1 in BG0001 without an aneurysm and with an aneurysm, Reynolds number 0.183 and 0.186 respectively and one LB area unit is $1.823 \cdot 10^{-10}$ m^2. Average mean shear stress increase is 3% (authors' own image)

The geometry P1 in BH0027 have an increase of WSS around the inserted aneurysm, which can be seen in figure 22b compared to 22a. This can be due to when the geometry was constructed with an aneurysm the edges of connection between the vessel and the aneurysm was sharp. Therefore it is numerical effects of the geometry which cause the higher WSS around the aneurysm.

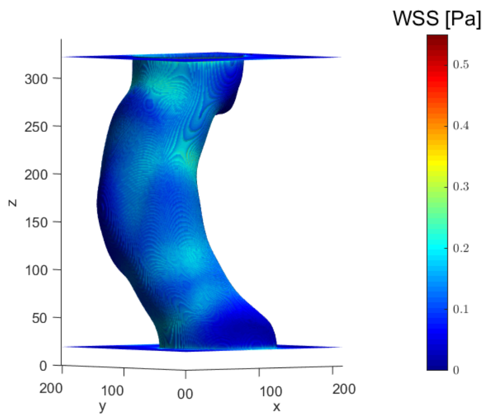

(a) Without aneurysm

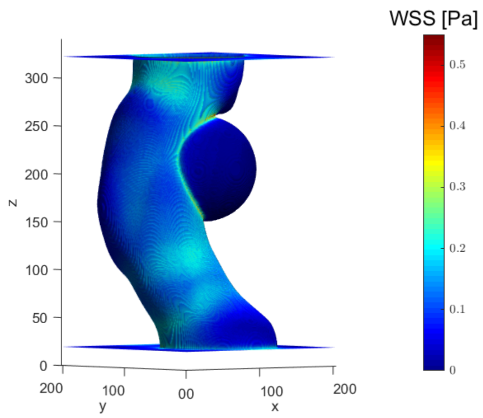

(b) With aneurysm

Figure 22: Wall shear stress for P1 in BH0027, without and with an aneurysm (authors' own images)

The mean shear stress regarding P1 in BH0027 without an aneurysm is higher with a decrease of the area, see figure 23. This also shows for the mean shear stress with an aneurysm because there is a decrease in the mean shear stress and an increase in the area due to the aneurysm. There is a global increase in the mean shear stress with the aneurysm.

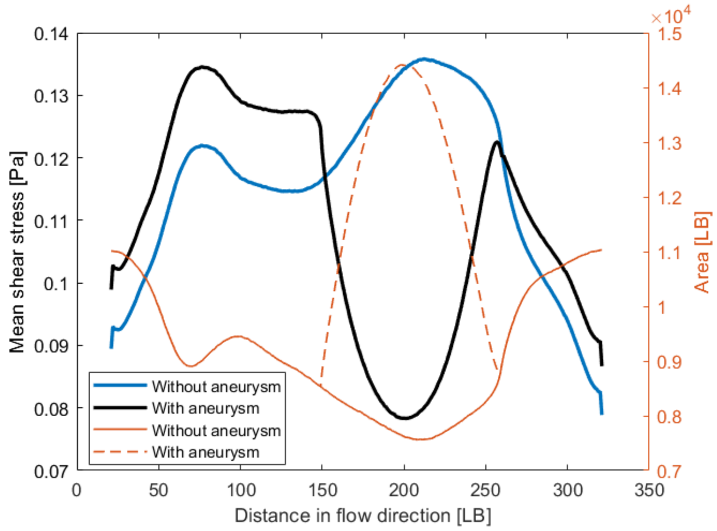

Figure 23: Mean shear stress for P1 in BH0027 without an aneurysm and with an aneurysm, Reynolds number 0.358 and 0.364 respectively and one LB area unit is $2.074 \cdot 10^{-10}$ m^2. Average mean shear stress increase is 10% (authors' own image)

The WSS of Rt ICA BH0027 can be seen in figure 24 and overall the values of the WSS is low since it is mostly blue in color. A few points can be seen to have higher WSS and for one of these points the aneurysm was inserted.

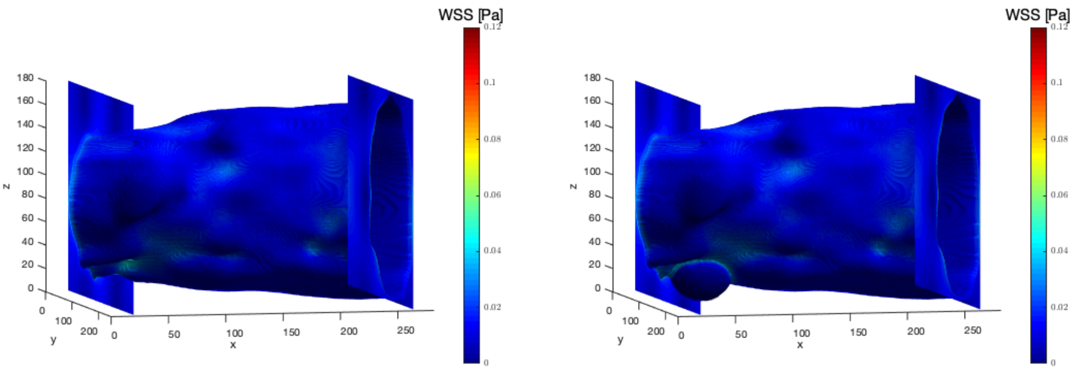

(a) Without aneurysm

(b) With aneurysm

Figure 24: Wall shear stress for Rt ICA in BH0027, without and with an aneurysm (authors' own images)

Figure 25 illustrates the mean shear stress and the cross-sectional area for Rt ICA BH0027. It can be seen that the highest mean shear stress occurs near the inlet. Due to lack of space, an aneurysm could not be inserted there. Inserting an aneurysm so close to the inlet would also cause it to intercept the buffer and in consequence possibly disrupt the function of the buffer.

There is a decrease in the mean shear stress as the cross-sectional area increases, which can be seen in figure 25. With an aneurysm inserted the global mean shear stress is higher. Previous geometries had shown a local decrease in mean shear stress for the aneurysm but not in this case. This could be due to the aneurysm area in relation to the geometry diameter. The insertion point is in a part of the geometry where the area increase is relatively high. This could result in the effects of the aneurysm not being as prominent because the increase in area is not as large.

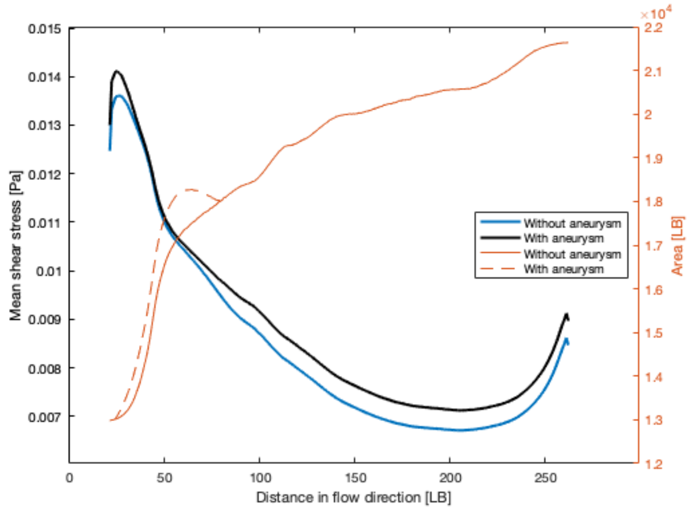

Figure 25: Mean shear stress for Rt ICA in BH0027 without an aneurysm and with an aneurysm, Reynolds number 0.329 and 0.347 respectively and one LB area unit is $7.896 \cdot 10^{-10}$ m^2. Average mean shear stress increase is 5% (authors' own image)

The geometry for ACom for BG0001 can be seen in figure 26 with the WSS, both without and with an aneurysm. One difference is the WSS by the aneurysm around 240 in x-direction, because it is higher than in the case without aneurysm.

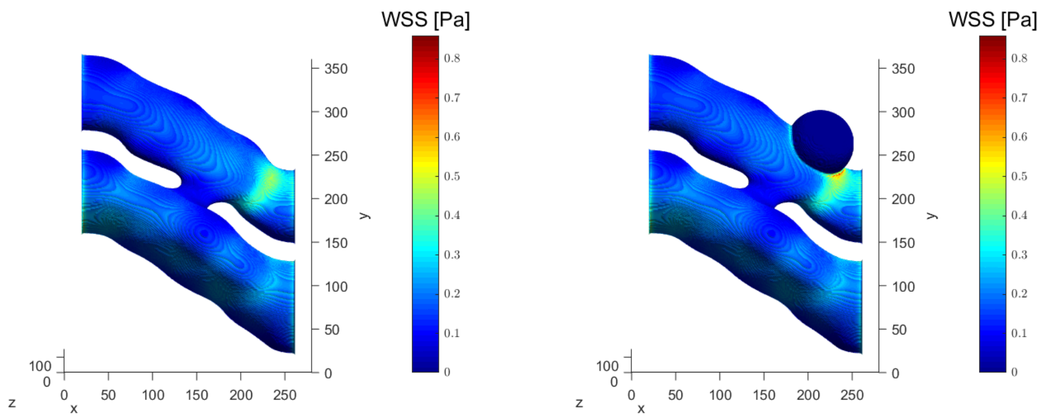

(a) Without aneurysm

(b) With aneurysm

Figure 26: Wall shear stress for ACom in BG0001, without and with an aneurysm (authors' own images)

The mean shear stress in figure 27 is locally lower where the aneurysm is inserted but from figure 26 it is higher WSS by the aneurysm. This can not be seen for the mean shear stress because it is an average and since the shear stress in the aneurysm is low the effect of the higher WSS is averaged out. There is a global increase for the case with an aneurysm.

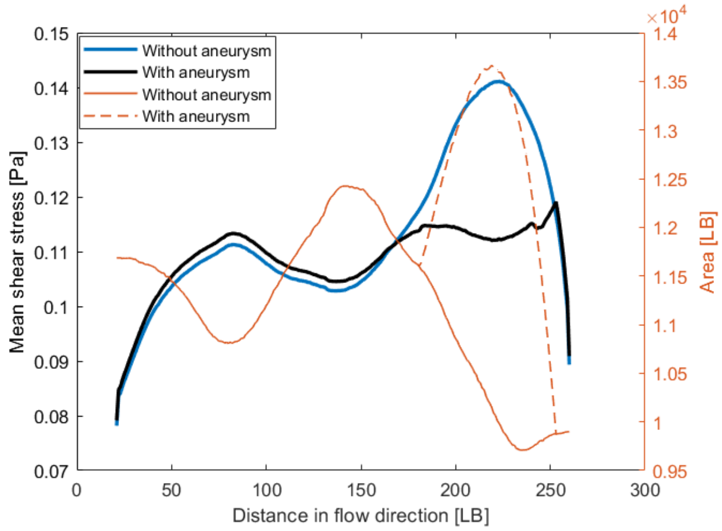

Figure 27: Mean shear stress for ACom in BG0001 without an aneurysm and with an aneurysm, Reynolds number 0.301 and 0.296 respectively and one LB area unit is $2.403 \cdot 10^{-10}$ m^2. Average mean shear stress increase is 2% (authors' own image)

The WSS of the ACom in BH0027 is shown in figure 28. In the figure it is possible to see a clear difference between the cases without and with aneurysm, with a higher WSS in the former case.

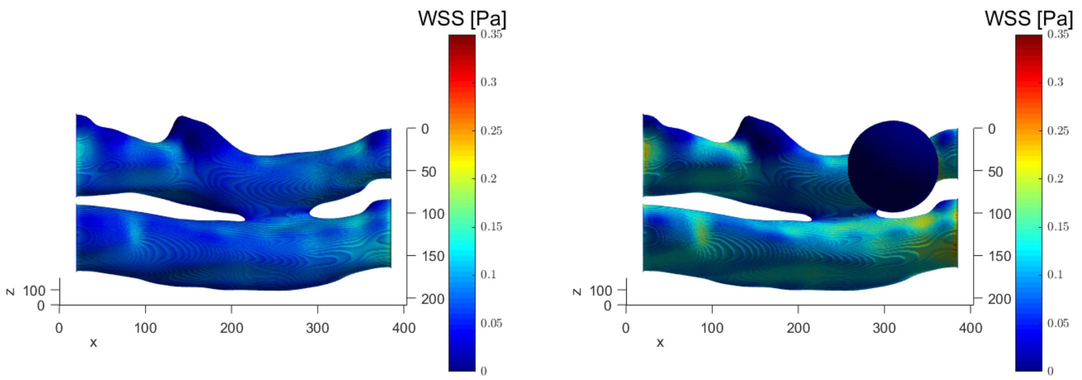

(a) Without aneurysm

(b) With aneurysm

Figure 28: Wall shear stress for ACom in BH0027, without and with an aneurysm (authors' own images)

Figure 29 shows the difference in mean shear stress between the cases. The difference is greatest directly after the aneurysm as seen in the previous geometries.

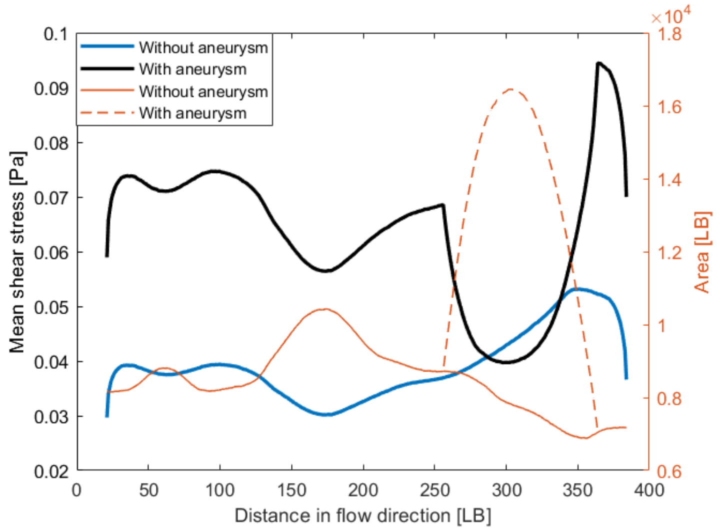

Figure 29: Mean shear stress for ACom in BH0027 without an aneurysm and with an aneurysm, Reynolds number 0.275 and 0.437 respectively and one LB area unit is $5.664 \cdot 10^{-10}$ $m^2$4. Average mean shear stress increase is 77% (authors' own image)

5.2 Comparison of Cross Sections Regarding Shear Stress, with and without a Constructed Aneurysm

The increase in shear stress, which occurs for most of the geometries, before and after the aneurysm insertion can be seen with cross sections of the shear stress for the geometries. Here the cross sections of P1 in BH0027 can be seen. A small increase of the shear stress can be seen when comparing figure 30a with 30b and figure 30e with 30f. These cross sections are located before and after the aneurysm. The flow near the wall of the aneurysm is stagnant which can be seen because the shear stress is zero near the wall, see figure 30d. Therefore the contours of the geometry is shown in the figures in order to see where the aneurysm is. As seen for the mean shear stress the shear stress is higher in the case without the aneurysm than with, see figure 30c and 30d. Cross sections for the remainder of the geometries can be seen in appendix B and the same stagnant flow near the aneurysm wall can be seen for all geometries.

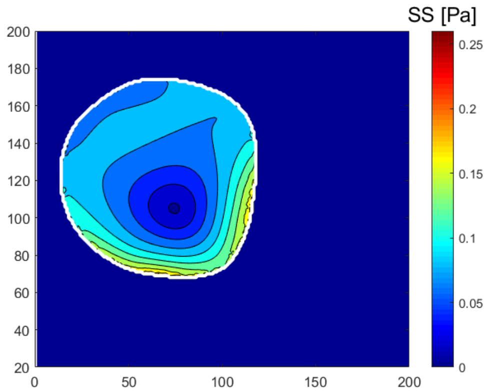

(a) Without aneurysm, cross section z = 116

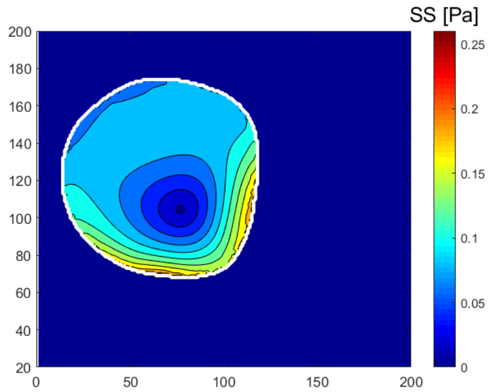

(b) With aneurysm, cross section at z = 116

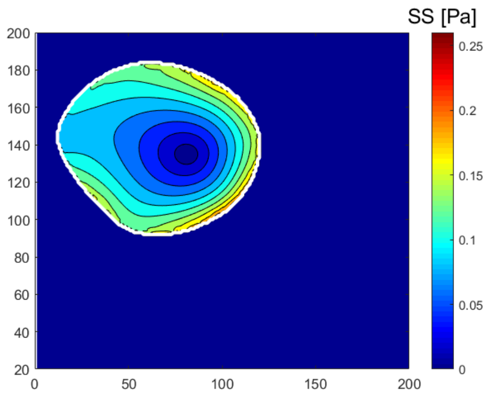

(c) Without aneurysm, cross section at z = 203

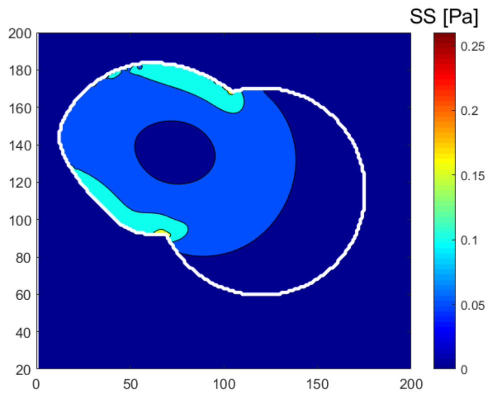

(d) With aneurysm, cross section at z = 203

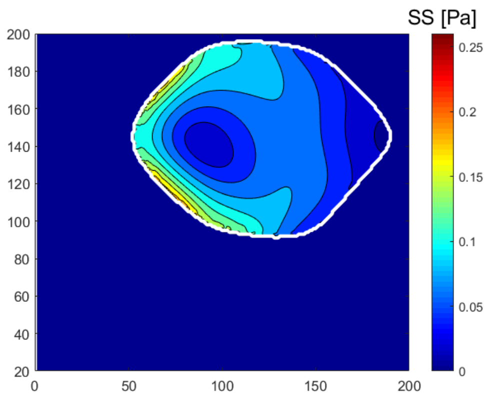

(e) Without aneurysm, cross section at z = 287

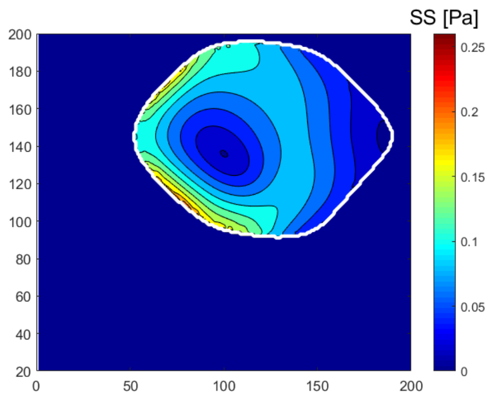

(f) With aneurysm, cross section at z = 287

Figure 30: Different cross sections in flow direction for the geometry P1 in BH0027, where SS is the shear stress (authors' own images)

6 Discussion

In this section of the report the results are discussed from multiple perspectives including the connection to medical aspects and the possibility to expand the research in the future. The accuracy of the model is reviewed with focus on sources of error. Furthermore the ethical consequences of the study are discussed.

The geometry plays a crucial role in the resulting shear stress which can be seen by the difference in shear stress between the cases with and without an aneurysm. It was also seen due to the difference in shear stress when comparing the geometries of the same region, for example P1, since the vascular systems between the brains have anatomical variations. Additionally, it can be seen that the cross-sectional area corresponds inversely with the mean shear stress. Since there is a varying cross-sectional area for the flow to pass through, the velocity changes accordingly which in turn affects the resulting shear stress.

In the tested geometries a global increase of the shear stress is observed after the insertion of an aneurysm. Therefore an aneurysm seems to alter the condition of the whole vessel and not only the part where it is expanding. Due to higher WSS correlating to the initial development of aneurysms, this could imply that the formation of one could be a cascading event that further destabilizes the cerebrovascular system. It is noteworthy however, that the magnitude of the WSS amplification is in certain simulations minimal, therefore conclusions on this subject would warrant further study within this field. However, assuming that this result can be replicated without some of the assumptions used in this report, it is a significant finding. These findings could point to the buildup of aneurysms as a system-wide affliction rather than a local one, and a self-propagating cascade at that.

The general flow environment of the geometries with inserted aneurysms displays similarities to previous studies that link aneurysm growth and rupture to low WSS, as described in section 3.3.2. The flow inside the aneurysms shows slow recirculating flow patterns, a type of secondary flow. Due to the geometry and placement of the inserted aneurysms, less blood flows into the aneurysm since the majority of the blood mostly follows the main direction of the blood vessel. The reduced blood flow inside the aneurysm causes blood stagnation and low WSS inside of it. In fact, the simulated results showed near zero velocities at the bottom of the aneurysm dome, with only a small recirculating flow in the dome. This aligns with general properties of Stokes flow, with small recirculation zones forming inside edges of cavities. At higher Reynolds number, the recirculation zone would still persist, but its shape and magnitude would be altered. The resulting flow patterns from the simulations therefore give a general idea of how the blood flows with an aneurysm present, and coincides with previous studies that have found low WSS inside aneurysms.

While the flow environment can vary a lot depending on the geometric structure of the blood vessel and its neighboring vessels, none of the geometries that are used in this project have any flow paths with impinging flow into an aneurysmal sac. The absence of impinging flows is also seen by the fact that no high WSS occurs inside any of the aneurysms, which is the prevalent effect from impinging flows.

The methodology for the simulations has been shown to be applicable for the purpose of calculating the shear stress for different geometries. It was also possible to modify the geometries by virtual insertion of aneurysms that were approximated as spheres. This could open up further possibilities of using other types of modifications on vascular reconstructions such as other classes or shapes of aneurysms, or studying other vascular disorders that affect the geometry of blood vessels. Therefore the methodology could be applied to research a wide range of vascular disorders other than just aneurysms.

6.1 Accuracy of Model

One factor that could have affected the results is the images from the MRI scans that served as a basis for the image reconstruction. The images from the MRI may not always be fully accurate if they contain noise or have missing details of the vessels. One solution to this could be to take several, repeated MRI scans of the same brain to see if the images would differ. The subsequent 3D reconstruction from the images could also have affected the results due to the manual choice of thresholds when extracting the vasculature. The chosen threshold values were considered optimal via tests of different values to observe which gave the clearest geometries. It was therefore a subjective choice and there is no guarantee of there being no noise or geometrical inadequacies in the reconstructed blood vessels. However, the geometries are still constructed from real MRI images and reflect the reality more than ideal models of blood vessels.

It is important to point out that simplifications have been made in the simulation of the velocity distribution. This includes the approximation of blood as a Newtonian fluid which contradicts the physical reality of blood flow. As described in section 4.3.1, the non-Newtonian effects on blood in larger arteries are mostly negligible. Yet, these simplifications will affect the final results and bring uncertainty to the connection between obtained results and the more complex reality.

Another approximation which may affect the accuracy of the model is the decision of the pressure gradient for the blood flow. This was chosen depending on the specific geometry and limited to only one direction, in reality the blood flows in a more complex way. The flow could occur in a diagonal direction and therefore in x-, y- and z-direction and this was not taken into consideration. One example of a diagonal flow can be seen in ACom in BG0001, see figure 7d. Here the flow is pushed solely in the x-direction, but the blood would actually flow in a more complex direction. The flow also needs to be pushed in either positive or negative direction. However, for these simulations the sign of the direction did not matter due to the approximation of Stokes flow, since this implies time-reversibility.

The fixed pressure gradient could be a source of error and could be a part of the reason for the observed increase in shear stress in the geometries, post aneurysm modification. This observation can be explained by the combination of equation (2) and an unchanging velocity profile in most of the geometry. This, since u_{avg} will increase with a constant $\frac{\partial P}{\partial x}$ and increasing area. The increased velocity in cross sections where the area has increased will then propagate out into the larger geometry, raising the overall mean velocity. Raising the mean velocity without changing the velocity profile, in most of the geometry, gives rise to a larger magnitude of shear stress. Hence, further research into this area is urged to do away with this pressure model and instead adopt, transient or not, pressure based boundary conditions.

6.2 Future Research

Future research could aim to compensate for some of the approximations used in this study. For example, the introduction of non-Newtonian fluid properties for blood would allow a more accurate representation of blood viscosity. When simulating a non-Newtonian fluid the blood viscosity is dependent upon the shear stress, and would therefore need to be iteratively updated as the solution is formed. This will predictably affect both the velocity and the shear stress profile, due to blood being shear-thinning.

Another topic for further research could revolve around the construction of a LBM model that does not use a fixed pressure gradient, and subsequently the implementation of a pulsating or transient flow. Pulsating or transient flow was not taken into consideration in this study since aneurysmal changes of the vascular system are usually not linked to sudden events, but rather something that develops over time. Hence it may seem reasonable to approximate blood flow as steady to study the time-averaged hemodynamic effects. While that assumption may seem reasonable, it could still be a dangerous simplification since it does not mirror the precise behavior of blood flow, and the pulsatile effects could play a bigger role than what is currently known.

Future research could also include comparisons with experimental measurements of the shear stress in order to further validate the observed effects. Another possibility could be to perform simulations on vessels with a real aneurysm instead of a constructed one. This could be of importance to see if the virtually constructed aneurysms correspond to the reality. However, this would require MRI images from a patient with a cerebral aneurysm, which was not acquired in this report.

Additionally, future research could include simulations with higher Reynolds values in order to be more representative of actual hemodynamic values for flow in arteries and veins. This would make it possible to compare numerical values with other external studies' results of velocity and WSS. Using higher Reynolds values with the current methodology and code used in this project would require more computational power and longer simulation times. Therefore it was not done for this study. If simulating with a higher Reynolds number the flow would not be defined as Stokes flow and therefore it is important that the direction of the fluid corresponds to the real flow direction in the vessels.

6.3 Ethics - The Use of *In Silico* Techniques as Alternatives to Animal Testing

The ethical aspects of animal testing within the scientific field have for a long time been a cause for controversy. *In vivo* testing that uses animals, has existed as a tool for medical and biological research since the dawn of medicine. It has led to significant discoveries and the development of modern day medicine. Arguments about the unethical treatment of animals in research have arisen in parallel, and guidelines and legislations have been created in response to this, with the intention of controlling the number of experiments conducted. Despite that, millions of animals still undergo experiments each year [60]. With the increased knowledge on how to simulate biological environments computationally, *in silico*, there is a possibility that the need for animal experiments is reduced. And in the future *in silico* may, along with *in vitro* testing, be developed enough to completely abolish animal testing.

A lot of important breakthroughs in medicine have been made possible due to the biological similarities between humans and animals. The development of vaccine or treatment of type 1 diabetes are examples of medical breakthroughs that would not have existed without the animal experiments that were conducted [61]. It ended up saving not only millions of humans, but also animals [62, 63], and shows that the use of animals has played a critical role in medicine.

However, animal testing does not always give correct results. Since physiological differences do exist between humans and animals, the results from animal experiments are not always applicable to humans. An example of this is the case of the drug thalidomide that had been tested on animals and therefore judged safe for humans. It led to devastating consequences; pregnant women who used it to combat nausea ended up giving birth to children with severe birth defects [64]. Due to the differences in physiology, a lot of studies that use animals still end up without any actual useful results because it is simply not possible to bridge the gap between animal and human [65].

Because of an increased consideration for animals in research, several guidelines and legislations have been put in place to minimize the amount of animal experiments or at the very least minimize their suffering. One common guiding principle is the "3Rs" that was created in 1959 by W. M. S. Russell and R. L. Burch [66]. It aims to instill humane use of animals in scientific research and consists of the three following objectives:

1. Use methods which avoid or replace the use of animals
2. Use methods that minimize the number of animals used for an experiment
3. Minimize the animals' suffering and improve their welfare

These three principles' connotations are imbued in several other guidelines and laws such as EU directives [67] and Sweden's animal protection law [68] whose contents are similar to what is stated in the 3Rs.

Using alternative methods, such as experiments *in silico* or *in vitro*, connects to the first principle of the 3Rs. In this project, no animals were directly used or harmed since the methods were done *in silico* through software simulations that reconstruct human vasculature. Indirectly though, certain values that have made the computational modeling possible were acquired from past research data that had experiments done on animals. Yet, knowledge and technology is developing fast, and while *in silico* techniques are often used in conjunction with values from *in vivo* experimentation, it could overall still reduce the use of animal experimenting if computational methods have enough data and become advanced enough to give full accuracy.

Another alternative form of testing is *in vitro*. It refers to the study of biological processes in controlled laboratory settings outside of their normal context. An example of this is the recent development of simulating the microarchitecture and function of living human organs on a small chip that inhabits a cell culture [69]. *In vitro* testing allows for a substance to be studied safely without animals or humans being subjected to the possible side effects, all the while having an increased accuracy because humans instead of animals can be examined. The drawback of *in vitro* is that it remains a challenge to extrapolate the results from *in vitro* back to the entire organism being studied, since a lot of biological interactions and networks were eliminated in the isolation process. Although if *in vitro* methods are developed accurately enough, it could end up being an optimal method to use along with *in silico* techniques and could grant far more accurate results than what can be obtained from animals.

Today, animals are still essential in medical research because alternative methods are not yet sufficient to fully replace the usefulness of animal models. However, if open and nuanced ethical discussions continue within the scientific field, along with legislations and guidelines that encourage the development of alternative methods, such as the one used in this project, a probable outcome could be a decrease in animal testing.

7 Conclusion

The aim of this work was to analyze the effects of a constructed aneurysm on the shear stress. To ensure credibility of the method a number of validations were made. In conclusion the validations showed, based on comparison with literature, that the methodology was considered useful for further simulations. The conclusion from the simulations is that the insertion of a constructed aneurysm in a blood vessel led to a global increase in shear stress for the selected geometries. Therefore the aneurysm did not only affect the local area where it was inserted but also had a global effect on the entire vessel. The global increase could lead to a cascading effect initiating more aneurysms. Future research could include compensation for the approximations made in this report, for example by investigating non-Newtonian fluid and simulations with higher Reynolds numbers.

References

[1] Mitchell MJ, King MR. Computational and Experimental Models of Cancer Cell Response to Fluid Shear Stress. Frontiers in Oncology. 2013;3:11. Available from: https://www.frontiersin.org/articles/10.3389/fonc.2013.00044/full.

[2] Castro MA. Understanding the Role of Hemodynamics in the Initiation, Progression, Rupture, and Treatment Outcome of Cerebral Aneurysm from Medical Image-Based Computational Studies. ISRN Radiology. 2013;Available from: https://www.ncbi.nlm.nih.gov/pmc/articles/PMC4045510/.

[3] Jeong W, Rhee K. Hemodynamics of cerebral aneurysms: computational analyses of aneurysm progress and treatment. Computational and mathematical methods in medicine. 2011;2012:1–11. Available from: https://www.ncbi.nlm.nih.gov/pmc/articles/PMC3290806/pdf/CMMM2012-782801.pdf.

[4] Shimogonya Y, Ishikawa T, Yamaguchi T, Kumamaru H, Itoh K. Computational Study of the Hemodynamics of Cerebral Aneurysm Initiation. In: Wu J, editor. Technological Advancements in Biomedicine for Healthcare Applications. IGI Global; 2013. p. 267–277. Available from: https://app.knovel.com/hotlink/pdf/id:kt00BHNJ51/technological-advancements/computatio-background.

[5] Maggiolo D. Lattice Boltzmann Method - a brief introduction and some applications [Permission to use]; 2017.

[6] Shojima M, Oshima M, Takagi K, Torii R, Hayakawa M, Katada K, et al. Magnitude and role of wall shear stress on cerebral aneurysm: Computational fluid dynamic study of 20 middle cerebral artery aneurysms. University of Tokyo; 2004. Available from: https://www.ahajournals.org/doi/pdf/10.1161/01.STR.0000144648.89172.0f.

[7] Kulcsá Z, Ugron A, Marosfo M, Berentei Z, Paá G, Szikora I. Hemodynamics of Cerebral Aneurysm Initiation: The Role of Wall Shear Stress and Spatial Wall Shear Stress Gradient. National Neuroscience Institute; 2010. Available from: http://www.ajnr.org/content/ajnr/32/3/587.full.pdf.

[8] The top 10 causes of death. World Health Organization; 2018. Available from: https://www.who.int/news-room/fact-sheets/detail/the-top-10-causes-of-death.

[9] Gasparotti R, Liserre R. Intracranial aneurysms. European Radiology. 2005;15(3):441–447. Available from: https://link.springer.com/content/pdf/10.1007%2Fs00330-004-2614-8.pdf.

[10] Sung-Nam H, Kyoung-Tae K, Taek-Kyun N. A Pseudoaneurysm Appeared after Rebleeding. Seoul: Department of Neurosurgery, College of Medicine, Chung-Ang University; 2007. Available from: https://www.jkns.or.kr/upload/pdf/0042007028.pdf.

[11] Sung Y. Magnetic Resonance Angiography Atlas Dataset; 2017. Available from: https://www.nitrc.org/projects/icbmmra/.

[12] R Welty J, L Rorrer G, G Foster D. Fundamentals of Momentum, Heat and Mass Transfer. 6th ed. Singapore: John Wiley & Sons; 2015.

[13] White FM. Fluid Mechanics. 8th ed. New York: McGraw-Hill Education; 2016.

[14] Kirby BJ. Stokes flow. In: Micro- and Nanoscale Fluid Mechanics: Transport in Microfluidic Devices. Cambridge University Press; 2009. Available from: http://www.kirbyresearch.com/textbook.

[15] Benny L. Creeping flow. In: Physics of Continuous Matter. 2nd ed. Copenhagen; 2004. p. 379 – 392. Available from: http://www.cns.gatech.edu/~predrag/GTcourses/PHYS-4421-04/lautrup/7.7/creep.pdf.

[16] Muhammad G, Shah NA. Calculation of Creeping Flow Past a Sphere Using Direct Boundary Element Method. Lahore: University of Engineering & Technology; 2010. 6. Available from: http://www.jofamericanscience.org/journals/am-sci/am0606/24_2500_sphere_am0606_162_165.pdf.

[17] Sochi T. Fluid Flow at Branching Junctions. International Journal of Fluid Mechanics Research. 2015;p. 1–33. Available from: http://arxiv.org/abs/1309.0227%0Ahttp://dx.doi.org/10.1615/InterJFluidMechRes.v42.i1.50.

[18] Gołosz J. Weak Interactions: Asymmetry of Time or Asymmetry in Time? Journal for General Philosophy of Science. 2017 3;48(1):19–33. Available from: http://link.springer.com/10.1007/s10838-016-9342-z.

[19] He X, Luo LS. Theory of the lattice Boltzmann method: From the Boltzmann equation to the lattice Boltzmann equation. PHYSICAL REVIEW E. 1997;56(6):6811–6817. Available from: https://journals.aps.org/pre/pdf/10.1103/PhysRevE.56.6811.

[20] Frisch U, D'humieres D, Hasslacher B, Lallemand P, Pomeau Y, Rivet JP. Lattice Gas Hydrodynamics in Two and Three Dimensions. Complex Systems. 1987;1(4):649–707. Available from: https://pdfs.semanticscholar.org/78f3/0e0bf1b77afd90be7f93dc6d7e88e3b4f453.pdf.

[21] Wu W, Huang X, Fang C, Gao Y. An improved MRT-LBM for Herschel–Bulkley fluids with high Reynolds number. Numerical Heat Transfer, Part B: Fundamentals. 2017;72(6):409–420. Available from: https://www.tandfonline.com/doi/full/10.1080/10407790.2017.1409521.

[22] Lallemand P, Luo LS. Theory of the lattice Boltzmann method: Dispersion, dissipation, isotropy, Galilean invariance, and stability. Phys Rev E. 2000 6;61(6):6546–6562. Available from: https://link.aps.org/doi/10.1103/PhysRevE.61.6546.

[23] Brownlee RA, Gorban AN, Levesley J. Stability and stabilization of the lattice Boltzmann method. Physical review E, Statistical, nonlinear, and soft matter physics. 2007;75. Available from: http://agorban.narod.ru/BGJPhyRev2007.pdf.

[24] Boyd J, Buick JM, Green S. A second-order accurate lattice Boltzmann nonNewtonian flow model. Journal of Physics A: Mathematical and General. 2006;39(46). Available from: https://doi.org/10.1088%2F0305-4470%2F39%2F46%2F001.

[25] Chai Z, Zhao TS. Effect of the forcing term in the multiple-relaxation-time lattice Boltzmann equation on the shear stress or the strain rate tensor. The Hong Kong University of Science and Technology; 2012. Available from: https://www.mae.ust.hk/~mezhao/pdf/177.pdf.

[26] Chandra A, Li WA, Stone CR, Geng X, Ding Y. The cerebral circulation and cerebrovascular disease I: Anatomy. Brain Circulation. 2017;3(2):45–56. Available from: https://www.ncbi.nlm.nih.gov/pmc/articles/PMC6126264/pdf/BC-3-45.pdf.

[27] Ethier CR, Simmons CA. The circulatory system. In: Introductory Biomechanics - From Cells to Organisms. Cambridge: Cambridge University Press; 2007. p. 179–204. Available from: https://app.knovel.com/hotlink/pdf/id:kt011CMV21/introductory-biomechanics/arterial-wall-structure.

[28] Iqbal S. A Comprehensive Study of the Anatomical Variations of the Circle of Willis in Adult Human Brains. Journal of Clinical and Diagnostic Research. 2013;7(11):2423–2427. Available from: https://www.ncbi.nlm.nih.gov/pmc/articles/PMC3879841/.

[29] Rhcastilhos Cs. Wikimedia commons - Circle of Willis;Available from: https://commons.wikimedia.org/w/index.php?title=File:Circle_of_Willis_es.svg&oldid=338292865.

[30] Karaman O, Şen M, Demirci EA. Electrospun scaffolds for vascular tissue engineering. In: Electrospun Materials for Tissue Engineering and Biomedical Applications: Research, Design and Commercialization. Elsevier Inc.; 2017. p. 261–287. Available from: https://app.knovel.com/hotlink/pdf/id:kt011FULE1/electrospun-materials/structure-blood-vessels.

[31] Zhang LG, Fisher JP, Leong KW. Blood vessel regeneration. In: 3D Bioprinting and Nanotechnology in Tissue Engineering and Regenerative Medicine. Oxford: Elsevier; 2015. p. 149–169. Available from: https://app.knovel.com/hotlink/pdf/id:kt00UR98F4/bioprinting-nanotechnology/blood-vess-introduction.

[32] Ayyaswamy PS. Introduction to Biofluid Mechanics. In: Fluid Mechanics. 4th ed. Oxford: Elsevier; 2008. p. 765–840. Available from: https://app.knovel.com/hotlink/pdf/id:kt0096RX71/fluid-mechanics-4th-edition/nature-blood-vessels.

[33] Davies PF. Flow-mediated endothelial mechanotransduction. Physiological Reviews. 1995 7;75(3):519–560. Available from: https://www.ncbi.nlm.nih.gov/pmc/articles/PMC3053532/pdf/nihms187596.pdf.

[34] Yeom E, Kang YJ, Lee SJ. Changes in velocity profile according to blood viscosity in a microchannel. Biomicrofluidics. 2014;8(3):1–11. Available from: https://www.ncbi.nlm.nih.gov/pmc/articles/PMC4162413/pdf/BIOMGB-000008-034110_1.pdf.

[35] Formaggia L, Quarteroni A, Veneziani A. Cardiovascular Mathematics - Modeling and simulation of the circulatory system. 1st ed. Quarteroni A, Hou T, Bris CL, Patera AT, Zuazua E, editors. Milano: Springer; 2009. Available from: https://link.springer.com/content/pdf/10.1007%2F978-88-470-1152-6.pdfhttps://books.google.se/books?hl=sv&lr=&id=BQpm2VDN3kcC&oi=fnd&pg=PR5&dq=Cardiovascular+Mathematics+-+Modeling+and+simulation+of+the+circulatory+system&ots=6U9gUlOmAs&sig=j2Qx83ecyffty2.

[36] Pruitt LA, Chakravartula AM. Cardiovascular devices. In: Mechanics of Biomaterials - Fundamental Principles for Implant Design. Cambridge: Cambridge University Press; 2011. p. 477–504. Available from: https://app.knovel.com/hotlink/pdf/id:kt0095RZX4/mechanics-biomaterials/cardiovascular-anatomy.

[37] Qiu T, Jin G, Xing H, Lu H. Association between hemodynamics, morphology, and rupture risk of intracranial aneurysms: a computational fluid modeling study. Neurological Sciences. 2017;38(6):1009–1018. Available from: https://link.springer.com/content/pdf/10.1007%2Fs10072-017-2904-y.pdf.

[38] Papaioannou TG, Stefanadis C. Vascular Wall Shear Stress: Basic Principles and Methods. Hellenic Journal of Cardiology. 2005;46(1):9–15. Available from: https://www.hellenicjcardiol.org/archive/full_text/2005/1/2005_1_9.pdf.

[39] Fung YC. The Flow Properties of Blood. In: Biomechanics: Mechanical Properties of Living Tissues. 2nd ed. New York: Springer; 1993. p. 66–108. Available from: https://link.springer.com/content/pdf/10.1007%2F978-1-4757-2257-4_3.pdf.

[40] Cebral JR, Putman CM, Alley MT, Hope T, Bammer R, Calamante F. Hemodynamics in Normal Cerebral Arteries: Qualitative Comparison of 4D Phase-Contrast Magnetic Resonance and Image-Based Computational Fluid Dynamics. Journal of engineering mathematics. 2009;64(4):367–378. Available from: https://www.ncbi.nlm.nih.gov/pmc/articles/PMC2726749/pdf/nihms109645.pdf.

[41] Retarekar R, Ramachandran M, Berkowitz B, Harbaugh RE, Hasan D, Rosenwasser RH, et al. Stratification of a Population of Intracranial Aneurysms Using Blood Flow Metrics. Comput Methods Biomech Biomed Engin. 2015;18(10):1072–1082. Available from: https://www.ncbi.nlm.nih.gov/pmc/articles/PMC4261052/pdf/nihms-562830.pdf.

[42] Sankar DS, Hemalatha K. A non-Newtonian fluid flow model for blood flow through a catheterized artery—Steady flow. Applied Mathematical Modelling. 2007;31(9):1847–1864. Available from: https://www.sciencedirect.com/science/article/pii/S0307904X06001569.

[43] Cherry EM, Eaton JK. Shear thinning effects on blood flow in straight and curved tubes. Physics of Fluids. 2013;25(7). Available from: https://aip.scitation.org/doi/full/10.1063/1.4816369.

[44] Sochi T. Non-Newtonian Rheology in Blood Circulation. London: University College London, Department of Physics & Astronomy; 2014. Available from: https://arxiv.org/pdf/1306.2067.pdf.

[45] Noutchie SCO. FLOW OF A NEWTONIAN FLUID THE CASE OF BLOOD IN LARGE ARTERIES. University of South Africa; 2005. Available from: http://uir.unisa.ac.za/bitstream/handle/10500/2234/dissertation.pdf;sequence=1.

[46] Jeong YG, Jung YT, Kim MS, Eun CK, Jang SH. Size and location of ruptured intracranial aneurysms. Journal of Korean Neurosurgical Society. 2009;45(1):11–15. Available from: https://www.ncbi.nlm.nih.gov/pmc/articles/PMC2640825/.

[47] Van Gijn J, Kerr RS, Rinkel GJE. Subarachnoid haemorrhage. wwwthelancetcom. 2007;369(9558):306–318. Available from: https://www.sciencedirect.com/science/article/pii/S0140673607601536.

[48] Williams LN, Brown RD. Management of unruptured intracranial aneurysms. Rochester: American Academy of Neurology; 2013. Available from: https://www.ncbi.nlm.nih.gov/pmc/articles/PMC3721237/pdf/CPJ200111.pdf.

[49] Finitsis S, Anxionnat R, Lebedinsky A, Albuquerque PC, Clayton MF, Picard L, et al. Endovascular Treatment of ACom Intracranial Aneurysms. Report on series of 280 Patients. Interv Neuroradiol. 2010;16(1):7–16. Available from: https://www.ncbi.nlm.nih.gov/pmc/articles/PMC3277962/pdf/IN-16-7.pdf.

[50] Kardile PB, Ughade JM, Pandit SV, Ughade MN. Anatomical Variations of Anterior Communicating Artery. Journal of clinical and diagnostic research. 2013;7(12):2661–2664. Available from: https://www.ncbi.nlm.nih.gov/pmc/articles/PMC3919289/.

[51] Gaillard APF. Anterior communicating artery;. Available from: https://radiopaedia.org/articles/anterior-communicating-artery?lang=us.

[52] Etminan N, Buchholz BA, Dreier R, Bruckner P, Torner JC, Steiger HJ, et al. Cerebral Aneurysms: Formation, Progression, and Developmental Chronology. Translational Stroke Research. 2014;5(2):167–173. Available from: https://www.ncbi.nlm.nih.gov/pmc/articles/PMC4399795/pdf/nihms677555.pdf.

[53] Sehba FA, Hou J, Pluta RM, Zhang JH. The importance of early brain injury after subarachnoid hemorrhage. Progress in Neurobiology. 2012 4;97(1):14–37. Available from: https://www.ncbi.nlm.nih.gov/pmc/articles/PMC3327829/pdf/nihms-362975.pdf.

[54] Desouza RM, Shah M, Koumellis P, Foroughi M. Subarachnoid haemorrhage secondary to traumatic intracranial aneurysm of the posterior cerebral circulation: case series and literature review. Acta Neurochirurgica. 2016;158(9):1731–1740. Available from: https://www.ncbi.nlm.nih.gov/pmc/articles/PMC4980416/pdf/701_2016_Article_2865.pdf.

[55] Rinkel GJE, Djibuti M, Algra A, van Gijn J. Prevalence and Risk of Rupture of Intracranial Aneurysms. Stroke. 1998;29(1):251–256. Available from: https://www.ahajournals.org/doi/pdf/10.1161/01.STR.29.1.251.

[56] Meng H, Tutino VM, Xiang J, Siddiqui A. High WSS or Low WSS? Complex interactions of hemodynamics with intracranial aneurysm initiation, growth, and rupture:

Toward a unifying hypothesis. American Journal of Neuroradiology. 2014;35(7):1254–1262. Available from: http://citeseerx.ist.psu.edu/viewdoc/download?doi=10.1.1.888.8519&rep=rep1&type=pdf.

[57] Sandoo A, Veldhuijzen Van Zanten JJCS, Metsios GS, Carroll D, Kitas GD. The Endothelium and Its Role in Regulating Vascular Tone; 2010. Available from: https://www.ncbi.nlm.nih.gov/pmc/articles/PMC3040999/pdf/TOCMJ-4-302.pdf.

[58] Meng H, Xiang J, Liaw N. The Role of Hemodynamics in Intracranial Aneurysm Initiation. International review of thrombosis. 2012;7:40–57. Available from: https://www.researchgate.net/publication/259147272_The_Role_of_Hemodynamics_in_Intracranial_Aneurysm_Initiation.

[59] Castro M, Putman C, Radaelli A, Frangi A, Cebral J. Hemodynamics and Rupture of Terminal Cerebral Aneurysms. Academic Radiology. 2009 10;16(10):1201–1207. Available from: http://www.ncbi.nlm.nih.gov/pubmed/19553143https://linkinghub.elsevier.com/retrieve/pii/S1076633209002578.

[60] Taylor K, Gordon N, Langley G, Higgins W. Estimates for worldwide laboratory animal use in 2005. The Humane Society Institute for Science and Policy; 2008. 3. Available from: https://animalstudiesrepository.org/cgi/viewcontent.cgi?referer=https://www.google.com/&httpsredir=1&article=1013&context=acwp_lab.

[61] Barré-Sinoussi F, Montagutelli X. Animal models are essential to biological research: issues and perspectives. Future Science OA. 2015 7;1(4). Available from: https://www.ncbi.nlm.nih.gov/pmc/articles/PMC5137861/pdf/fso-01-63.pdf.

[62] Greenwood B. The contribution of vaccination to global health: Past, present and future. London: Royal Society of London; 2014. Available from: https://www.ncbi.nlm.nih.gov/pmc/articles/PMC4024226/pdf/rstb20130433.pdf.

[63] Karamanou M. Milestones in the history of diabetes mellitus: The main contributors. World Journal of Diabetes. 2016 1;7(1):1–7. Available from: https://www.wjgnet.com/1948-9358/full/v7/i1/1.htm.

[64] Greek R, Shanks N, Rice MJ. The History and Implications of Testing Thalidomide on Animals; 2011. 3. Available from: http://jpsl.org/archives/history-and-implications-testing-thalidomide-animals/.

[65] AKHTAR A. The Flaws and Human Harms of Animal Experimentation. Cambridge Quarterly of Healthcare Ethics. 2015 9;24(4):407–419. Available from: https://www.ncbi.nlm.nih.gov/pmc/articles/PMC4594046/.

[66] National Centre for the Replacement Refinement & Reduction of Animals in Research. The 3Rs; 2019. Available from: https://www.nc3rs.org.uk/the-3rs.

[67] Official Journal of the European Union. DIRECTIVE 2010/63/EU OF THE EUROPEAN PARLIAMENT AND OF THE COUNCIL of 22 September 2010 on the protection of animals used for scientific purposes. 2010;p. 33–79. Available from: https://eur-lex.europa.eu/LexUriServ/LexUriServ.do?uri=OJ:L:2010:276:0033:0079:en:PDF.

[68] Djurskyddslag SFS 2018:1192;.

[69] Ingber DE. Developmentally inspired human 'organs on chips'. Development. 2018 5;145(16):1–4. Available from: http://dev.biologists.org/content/develop/145/16/dev156125.full.pdf.

A Validation Results

Additional validation results can be seen in this section, this is regarding both two-dimensional and three-dimensional validation. The rest of the cases from table 3 which are not shown in section 4.4.1 can be seen. Furthermore, the remainder of the cases corresponding to the chosen geometries, see table 4, can also be seen. The three-dimensional cases shown are the rest of table 5 which are not shown in section 4.4.2.

A.1 Two-Dimensional Validation

The velocity profiles for flow between two parallel plates have an increasing maximum value with an increasing buffer length. The slope of the shear stress profiles is also increasing with a higher value of buffer length. This can be seen in both figure 31 and 32 for plate length 151 and 201 LB-nodes, respectively. Both cases with a diameter of 21 LB-nodes and for a cross section in the middle of the plate length.

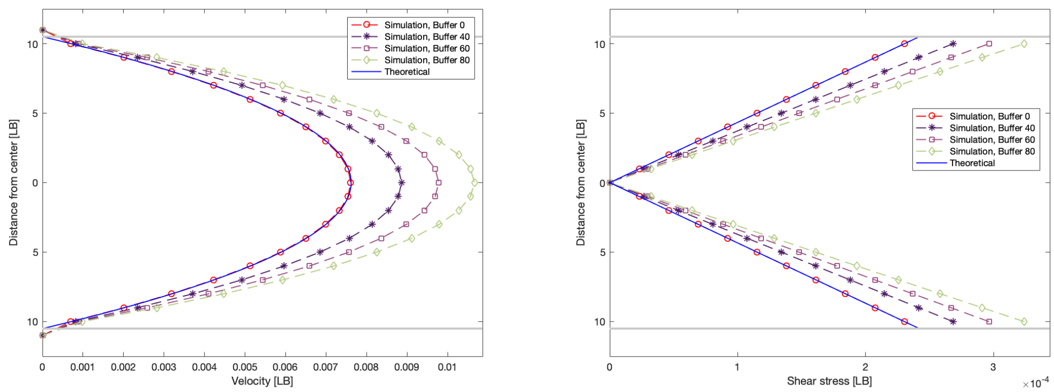

(a) Velocity profiles

(b) Shear stress profiles

Figure 31: Velocity profiles and shear stress profiles between two parallel plates for a cross section in the middle of the plate for different buffer lengths with a plate length of 151 and a diameter of 21 LB-nodes (authors' own images)

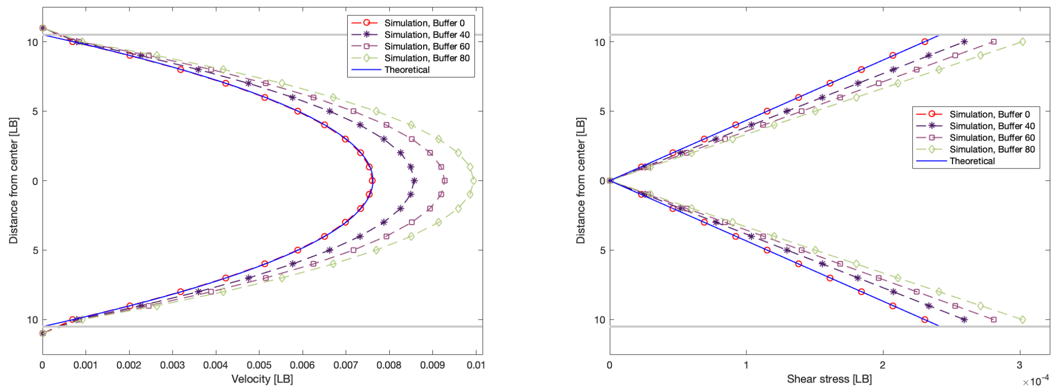

(a) Velocity profiles

(b) Shear stress profiles

Figure 32: Velocity profiles and shear stress profiles between two parallel plates for a cross section in the middle of the plate for different buffer lengths with a plate length of 201 and a diameter of 21 LB-nodes (authors' own images)

In figure 33 the velocity profiles and shear stress profiles can be seen for two different plate lengths, 101 and 201 LB-nodes, with a diameter of 41 LB-nodes. With an increasing diameter and therefore an increasing ratio between the plate length and the diameter, the velocity profile is closer to the theoretical profile in magnitude. This applies both to the velocity and shear stress profile.

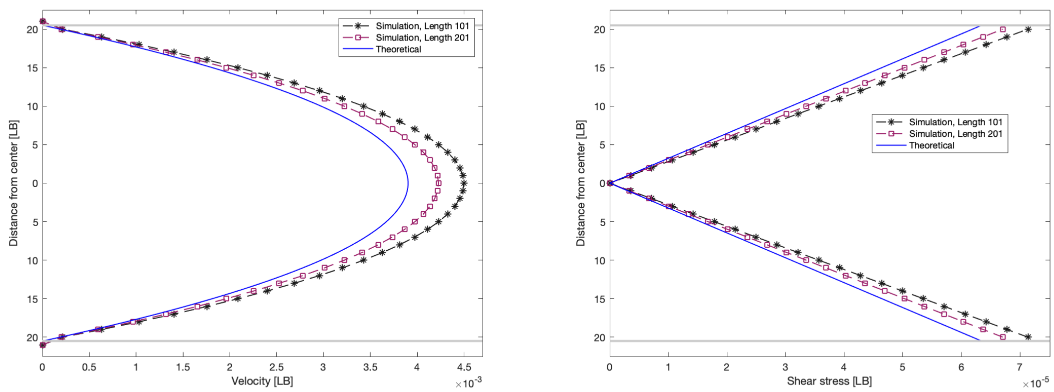

(a) Velocity profiles

(b) Shear stress profiles

Figure 33: Velocity profiles and shear stress profiles between two parallel plates for a cross section in the middle of the plate for different plate lengths, 101 and 201 LB-nodes, a diameter of 41 and a buffer length of 40 LB-nodes (authors' own images)

A parabolic velocity profile was obtained for the different cases regarding flow between two parallel plates. This can be seen in figures 34-36 for the ratios corresponding to the chosen geometries except for P1, both in BG0001 and BH0027, which can be seen in figure 13 instead. A small difference between the simulated cases and the theoretical profiles can be seen.

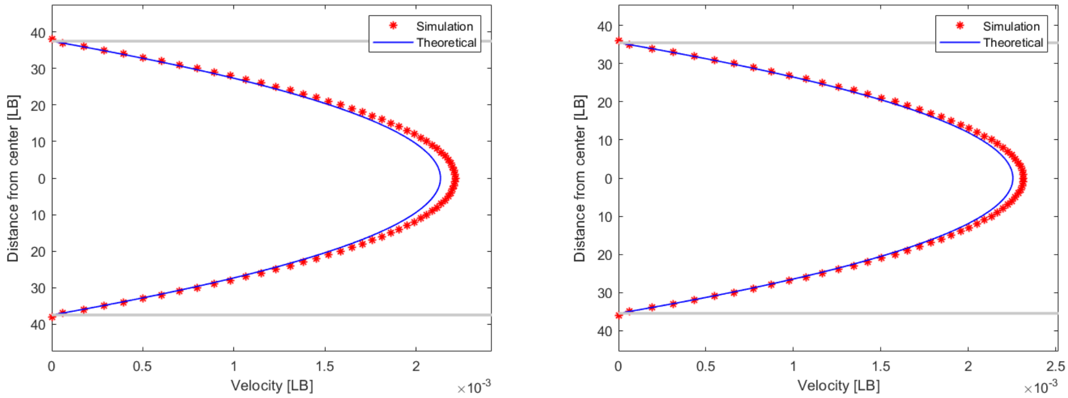

(a) ACom - BG0001

(b) ACom - BH0027

Figure 34: Velocity profiles between two parallel plates with ratios corresponding to ACom in both brains, for a cross section in the middle of the length (authors' own images)

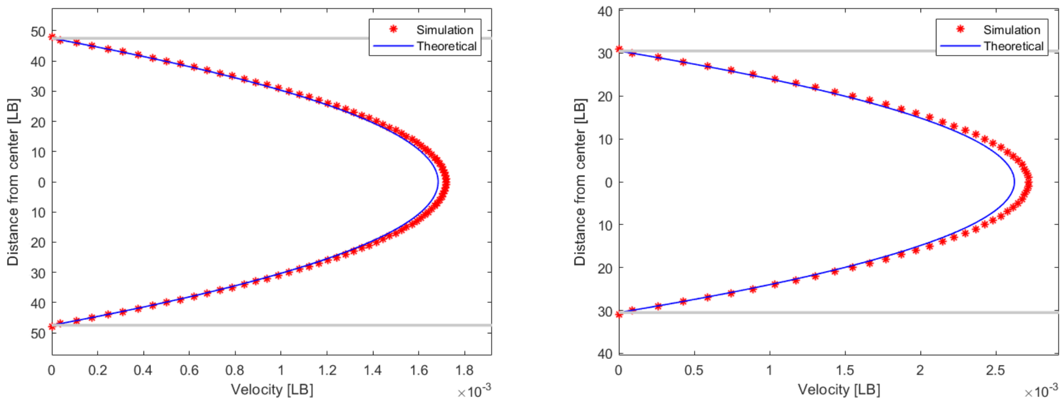

(a) Branching - BG0001

(b) Curvature - BG0001

Figure 35: Velocity profiles between two parallel plates with ratios corresponding to branching and curvature in BG0001, for a cross section in the middle of the length (authors' own images)

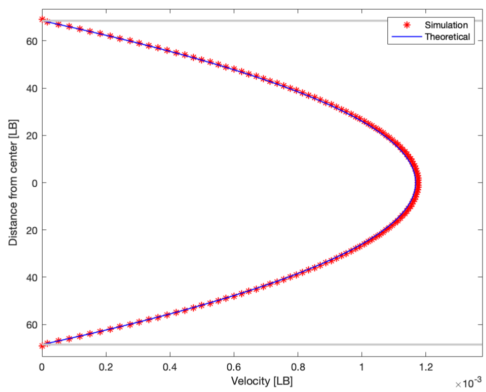

Figure 36: Velocity profiles between two parallel plates with ratios corresponding to Rt ICA, BH0027, for a cross section in the middle of the length (authors' own image)

A.2 Three-Dimensional Validation

Figures 37 and 38 shows the velocity profiles and shear stress profiles for two three-dimensional pipes with different length and diameter. Both cases were without a buffer. A small deviation between the simulated and the theoretical velocity profiles can be seen, particularly near the wall. There is a difference between the simulated and theoretical shear stress profiles closer to the wall, the simulated profiles show a decrease in shear stress near the wall. The difference both in velocity profiles and shear stress profiles are due to an uneven geometry shape, which can be seen in figure 15 for a similar pipe.

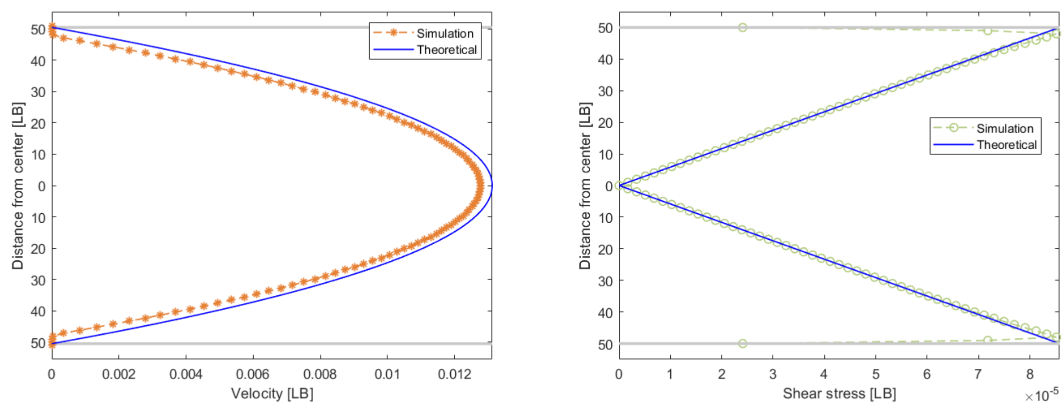

(a) Velocity profiles (b) Shear stress profiles

Figure 37: Velocity profiles and shear stress profiles in a 3D pipe for a cross section in the middle of the pipe in length and height direction, length 301 and diameter 101 LB-nodes (authors' own images)

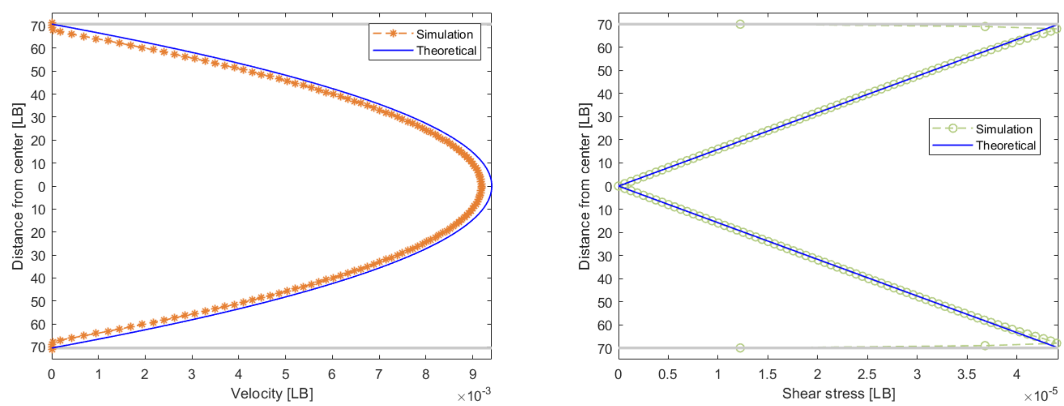

(a) Velocity profiles (b) Shear stress profiles

Figure 38: Velocity profiles and shear stress profiles in a 3D pipe for a cross section in the middle of the pipe in length and height direction, length 281 and diameter 141 LB-nodes (authors' own images)

B Cross Sections with Shear Stress in the Chosen Geometries

Cross sections before, in the middle of and after the aneurysm is shown here for all geometries except for P1 in BH0027, see figure 30 in section 5. For all inserted aneurysms the shear stress is zero near the aneurysm wall and therefore it can be seen that the flow is stagnant at these locations. For ACom in BH0027 the increase in shear stress before and after the aneurysms can be seen, see figure 43.

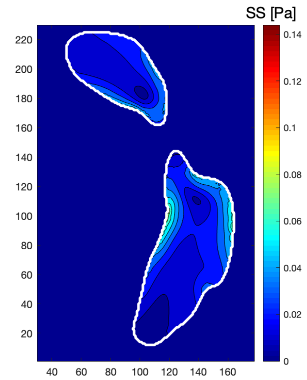

(a) Without aneurysm, cross section z = 35

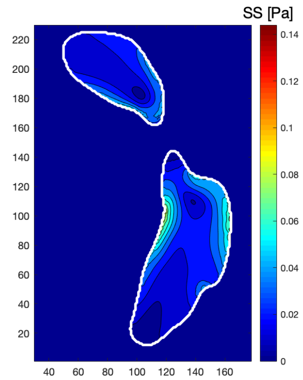

(b) With aneurysm, cross section at z = 35

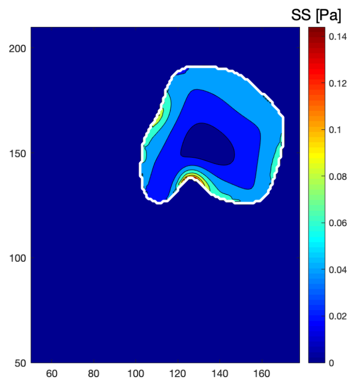

(c) Without aneurysm, cross section at z = 113

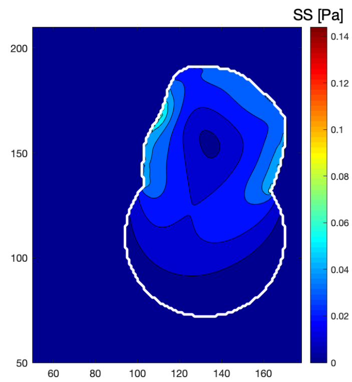

(d) With aneurysm, cross section at z = 113

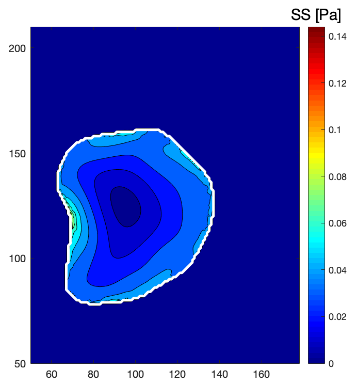

(e) Without aneurysm, cross section at z = 254

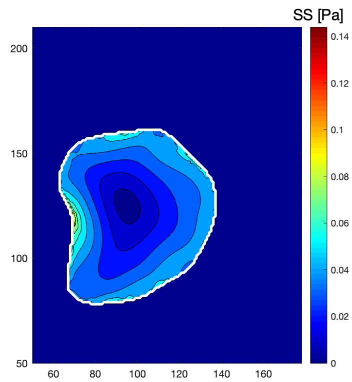

(f) With aneurysm, cross section at z = 254

Figure 39: Different cross sections in flow direction for the geometry bifurcation at Rt ICA in BG0001, where SS is the shear stress (authors' own images)

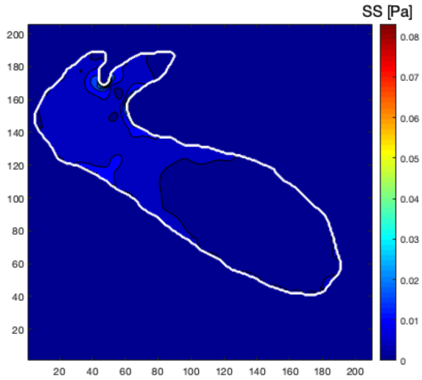

(a) Without aneurysm, cross section at y = 132

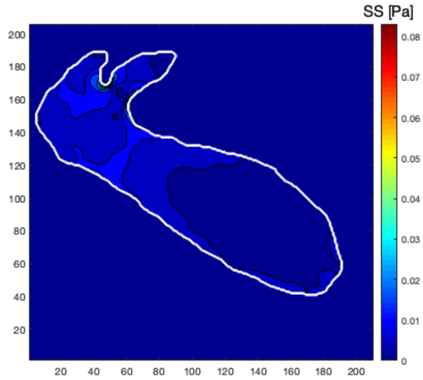

(b) With aneurysm, cross section at y = 132

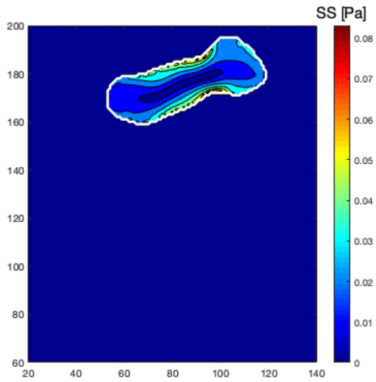

(c) Without aneurysm, cross section at y = 188

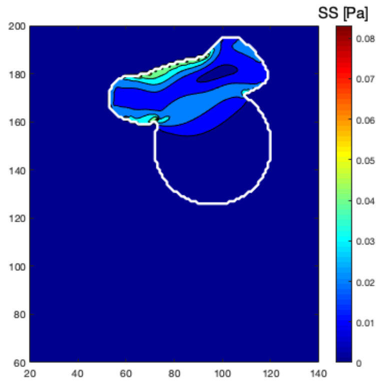

(d) With aneurysm, cross section at y = 188

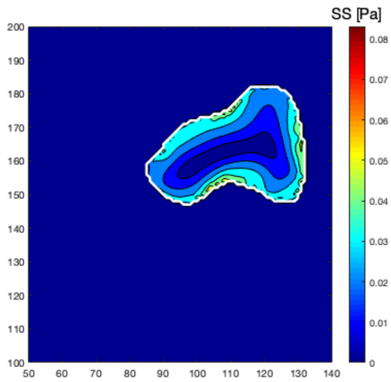

(e) Without aneurysm, cross section at y = 230

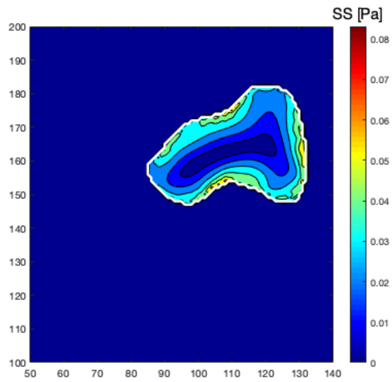

(f) With aneurysm, cross section at y = 230

Figure 40: Different cross sections in flow direction for the geometry curvature at Rt ICA in BG0001, where SS is the shear stress (authors' own images)

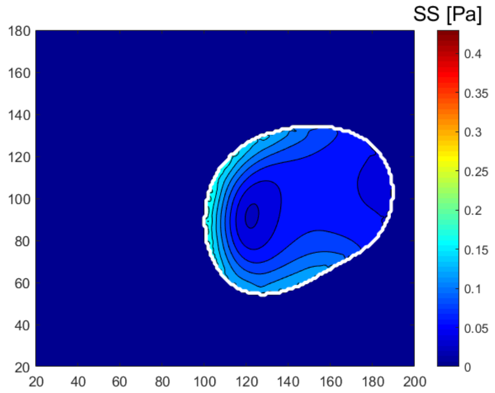

(a) Without aneurysm, cross section z = 35

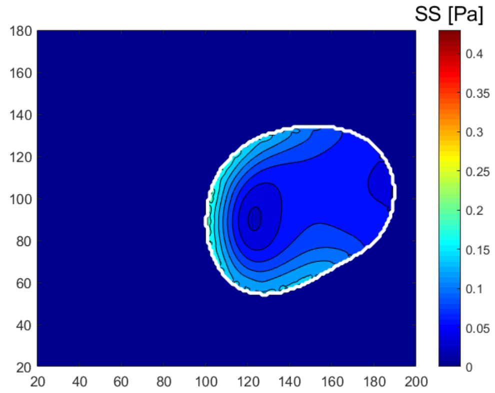

(b) With aneurysm, cross section at z = 35

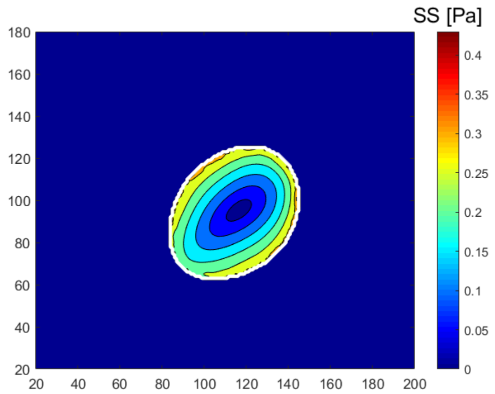

(c) Without aneurysm, cross section at z = 95

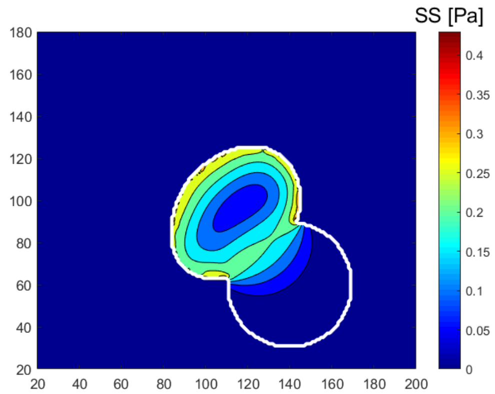

(d) With aneurysm, cross section at z = 95

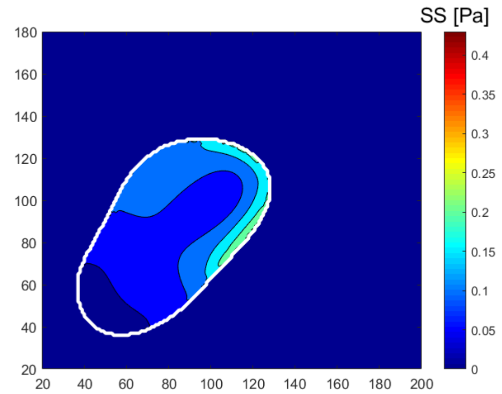

(e) Without aneurysm, cross section at z = 160

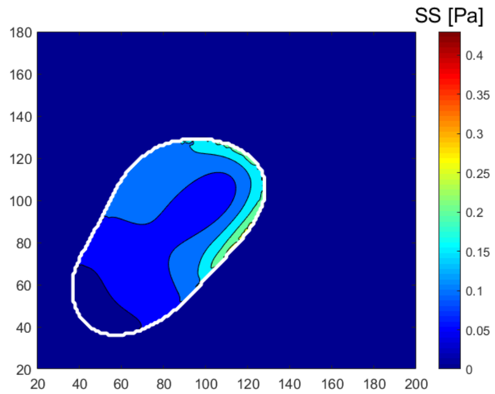

(f) With aneurysm, cross section at z = 160

Figure 41: Different cross sections in flow direction for the geometry P1 in BG0001, where SS is the shear stress (authors' own images)

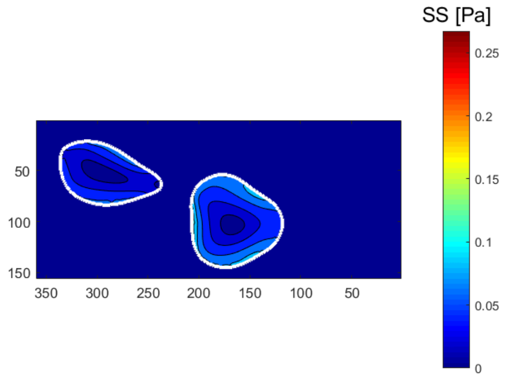

(a) Without aneurysm, cross section x = 82

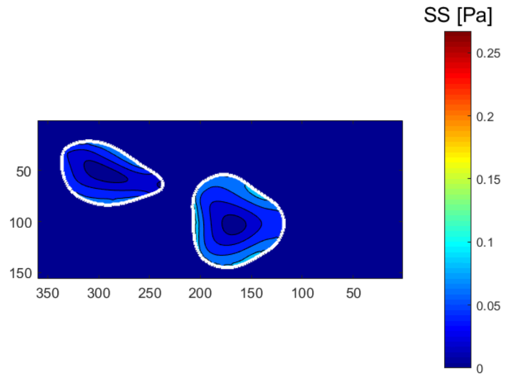

(b) With aneurysm, cross section at x = 82

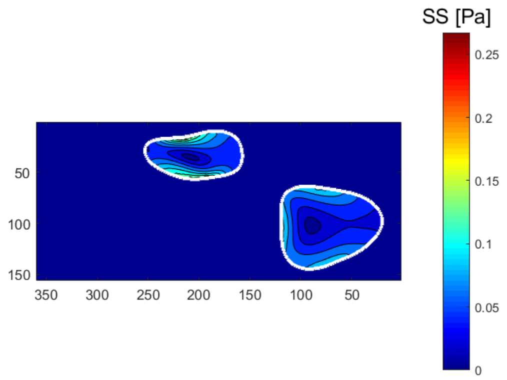

(c) Without aneurysm, cross section at x = 222

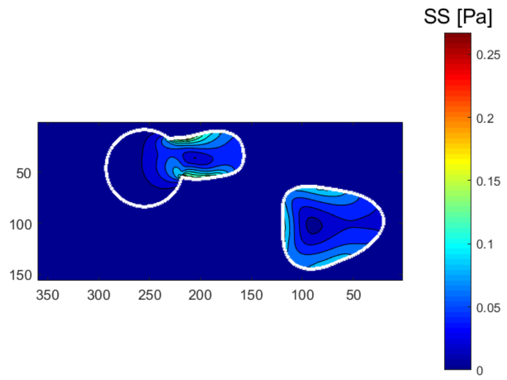

(d) With aneurysm, cross section at x = 222

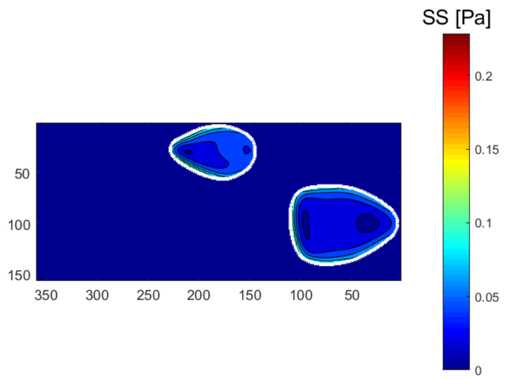

(e) Without aneurysm, cross section at x = 255

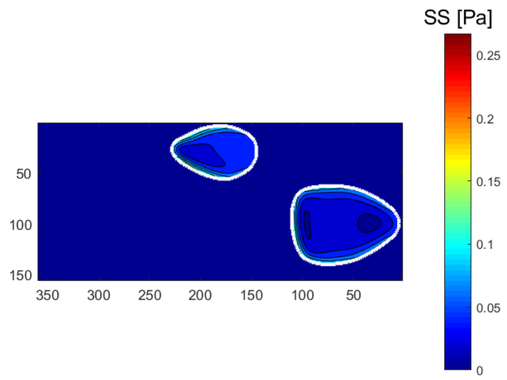

(f) With aneurysm, cross section at x = 255

Figure 42: Different cross sections in flow direction for the geometry ACom in BG0001, where SS is the shear stress (authors' own images)

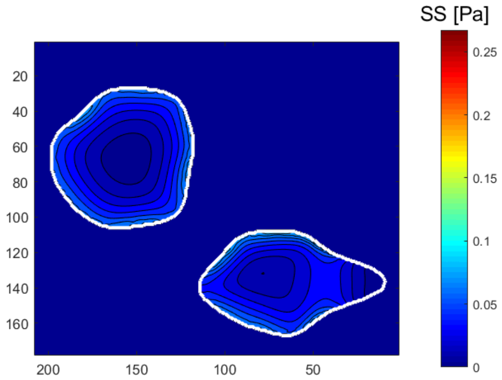

(a) Without aneurysm, cross section x = 141

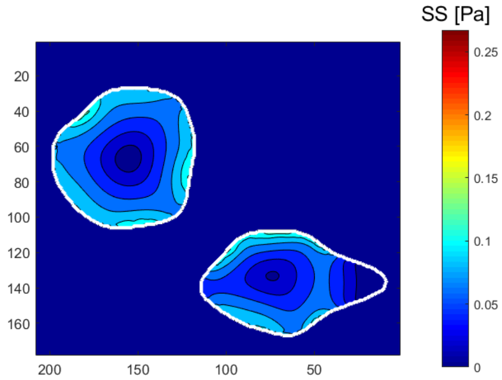

(b) With aneurysm, cross section at x = 141

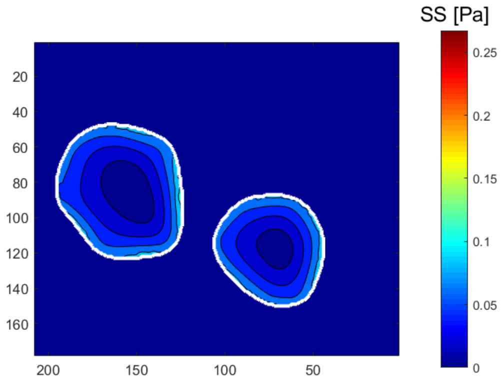

(c) Without aneurysm, cross section at x = 320

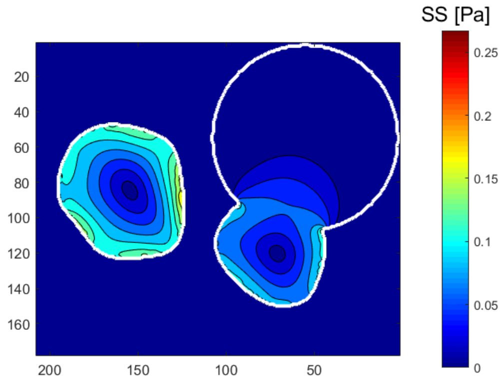

(d) With aneurysm, cross section at x = 320

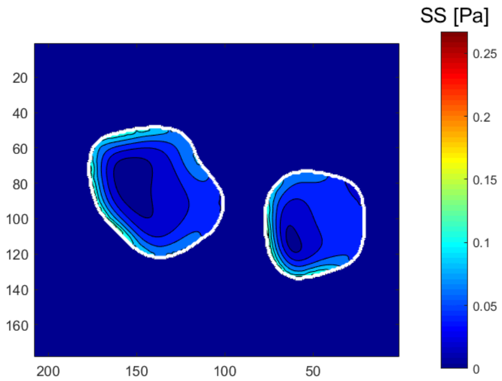

(e) Without aneurysm, cross section at x = 372

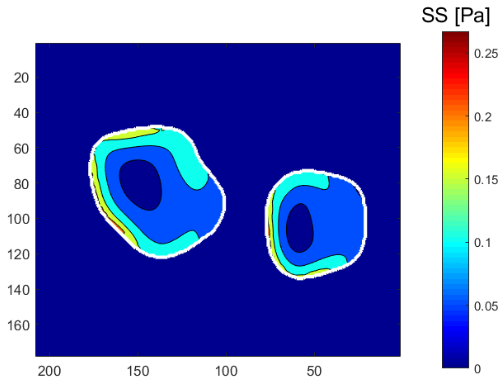

(f) With aneurysm, cross section at x = 372

Figure 43: Different cross sections in flow direction for the geometry ACom in BH0027, where SS is the shear stress (authors' own images)

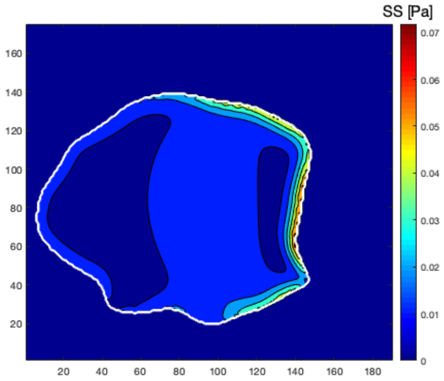

(a) Without aneurysm, cross section x = 26

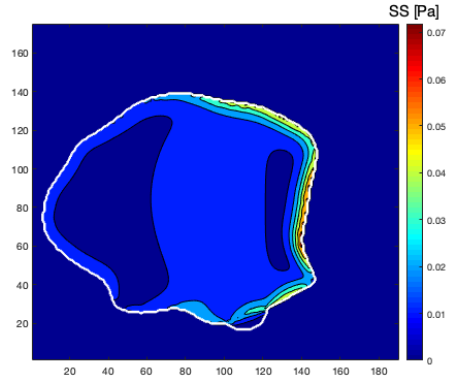

(b) With aneurysm, cross section at x = 26

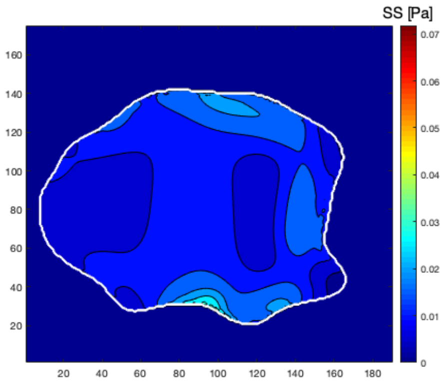

(c) Without aneurysm, cross section at x = 42

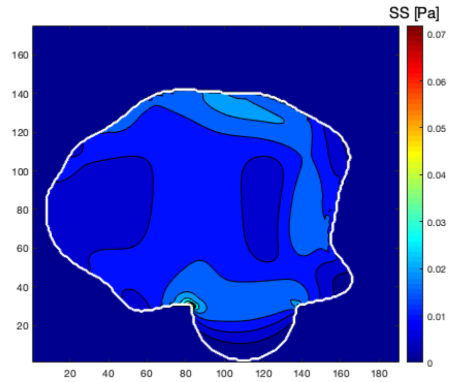

(d) With aneurysm, cross section at x = 42

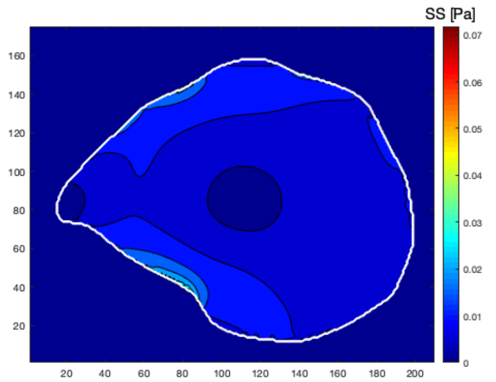

(e) Without aneurysm, cross section at x = 94

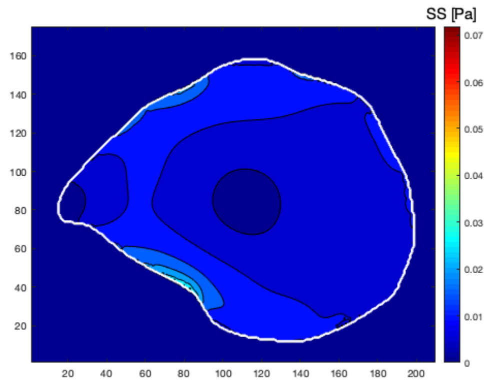

(f) With aneurysm, cross section at x = 94

Figure 44: Different cross sections in flow direction for the geometry Rt ICA in BH0027, where SS is the shear stress (authors' own images)